

TFusionOcc: Student's t-Distribution Based Object-Centric Multi-Sensor Fusion Framework for 3D Occupancy Prediction

Zhenxing Ming, Julie Stephany Berrio, Mao Shan, and Stewart Worrall

Abstract—3D semantic occupancy prediction enables autonomous vehicles (AVs) to perceive fine-grained geometric and semantic structure of their surroundings from onboard sensors, which is essential for safe decision-making and navigation. Recent models for 3D semantic occupancy prediction have successfully addressed the challenge of describing real-world objects with varied shapes and classes. However, the intermediate representations used by existing methods for 3D semantic occupancy prediction rely heavily on 3D voxel volumes or a set of 3D Gaussians, hindering the model's ability to efficiently and effectively capture fine-grained geometric details in the 3D driving environment. This paper introduces TFusionOcc, a novel object-centric multi-sensor fusion framework for predicting 3D semantic occupancy. By leveraging multi-stage multi-sensor fusion, Student's t-distribution, and the T-Mixture model (TMM), together with more geometrically flexible primitives, such as the deformable superquadric (superquadric with inverse warp), the proposed method achieved state-of-the-art (SOTA) performance on the nuScenes benchmark. In addition, extensive experiments were conducted on the nuScenes-C dataset to demonstrate the robustness of the proposed method in different camera and lidar corruption scenarios. The code will be available at: <https://github.com/DanielMing123/TFusionOcc>

Index Terms—Autonomous driving, 3D semantic occupancy prediction, Multi-sensor fusion, Environment perception

I. INTRODUCTION

Accurate and efficient modeling of the scene around autonomous vehicles (AV) is essential for safe and collision-free navigation. As technology advances, the introduction of a 3D semantic occupancy representation has successfully addressed the limitations of traditional 3D object detection and 2D bird's-eye-view (BEV) segmentation networks, particularly for detecting irregular objects and predicting occupied space in 3D. Thus, 3D semantic occupancy provides a suitable representation of the vehicle's surrounding environment. This representation inherently ensures geometric consistency of the AV's driving scene and can accurately describe occluded areas. In addition, a multi-sensor fusion technique for 3D semantic occupancy prediction further enhances an AVs' ability to model the 3D world.

Recent advances in voxel-based multi-sensor fusion methods [1]–[7] have achieved remarkable progress by integrating complementary information from different sensors, such as surround-view cameras, surround-view radars, and lidars.

This work has been supported by the Australian Centre for Robotics (ACFR). The authors are with the ACFR at the University of Sydney (NSW, Australia). E-mails: zmin2675@uni.sydney.edu.au, {j.berrio, m.shan, s.worrall}@acfr.usyd.edu.au

Demonstrating superior robustness and overall performance in several challenging light and weather conditions, these methods heavily rely on volumetric grid calculations (Fig 1, voxel-based approach), which hinders real-time application and makes them unsuitable for edge device deployment. Meanwhile, recent advances in object-centric multi-sensor fusion methods [8], [9] aim to address the limitations of the voxel-based approach by utilizing a set of 3D Gaussian primitives to only model the occupied area in the driving scene (Fig 1, 3D Gaussian-based approach), reducing the computational overhead caused by empty regions by concentrating representational capacity where it matters most. However, their modeling performance is inferior to that of voxel-based approaches. This performance gap is mainly due to the limited geometric shape representation capability of primitives and their weaker robustness to outliers.

To address the aforementioned limitations, we propose TFusionOcc (Fig 1, our approach), a novel Student's t-distribution-based object-centric multi-sensor fusion framework. We adopt a multi-stage feature-level fusion strategy, including early-stage, middle-stage, and late-stage fusion, to better integrate complementary information across modalities and mitigate the drawbacks of each modality. For object-centric modeling, we adopt a Student's t-distribution and the T-Mixture model (TMM) as a probability kernel, combined with several types of primitives, such as the general T-Primitive, superquadric, and deformable superquadric (superquadric with inverse-warp), to achieve greater geometric shape representation flexibility and robustness against outliers. The extensive experiments conducted on nuScenes [10] and nuScenes-C [11] datasets demonstrate that our proposed approach not only achieves state-of-the-art (SOTA) performance but also exhibits superior robustness against several sensor corruptions. The main contributions of this paper are summarized as follows:

- We propose TFusionOcc, a novel object-centric multi-stage multi-sensor fusion framework that leverages different types of T primitives to efficiently and effectively model the 3D driving scene for 3D semantic occupancy prediction.
- We propose a multi-gate cross-attention fusion module (MGCAFusion), which consists of a weighted summation and gated concatenation fusion modules, to combine the multi-modal features in an effective way.
- We propose a set of Student's t-distribution-based primitives, including the general T-Primitive, the T-

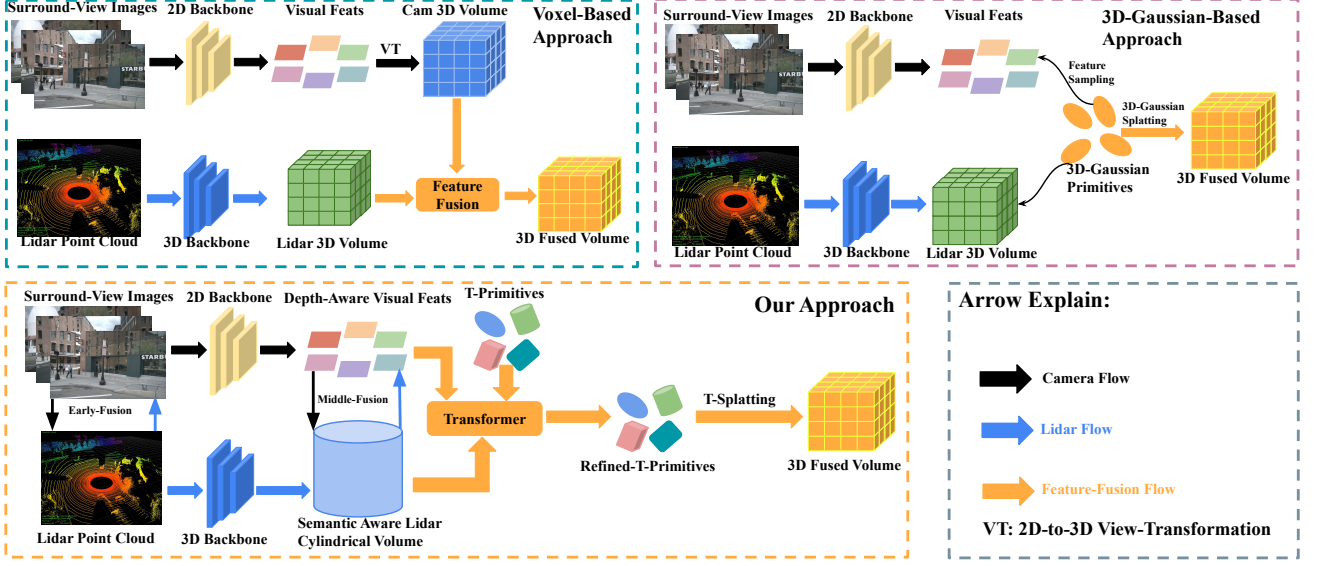


Fig. 1: **Pipeline of three approaches:** Voxel-based approach (top-left), 3D-Gaussian-Primitive-based object-centric approach (top-right), and our approach (bottom-left).

Superquadric primitive, and the T-Superquadric with inverse warp primitive, to effectively model 3D driving scenes.

- We thoroughly investigated the robustness of the proposed method with respect to the impact of different perception ranges and different lidar and camera corruption scenarios.

The remainder of this paper is structured as follows. Section II provides an overview of related research and identifies the key differences between this study and previous publications. Section III outlines the general framework of TFusionOcc and offers a detailed explanation of the implementation of each module. Section IV presents the results of our experiments. Finally, Section V provides the conclusion of our work.

II. RELATED WORK

A. Voxel-Based Approach

In OccFusion [1], the authors extract a set of 3D voxel volumes from each different modality sensor, such as surround-view cameras, surround-view radars and lidar, followed by the feature fusion operation through the proposed dynamic feature fusion module to perform multi-sensor fusion-based 3D semantic occupancy prediction. The model exhibits strong robustness under challenging rain and night scenarios. In Co-Occ [2], the authors leverage the volume rendering technique, which originally derived from NeRF [12], to refine the intermediate 3D feature volumes. They also proposed a GSFusion module for efficient multimodal feature fusion, achieving SOTA performance. In OccCylindrical [4], the authors proposed a multi-sensor fusion-based framework that uses a cylindrical partition to perform voxelisation of a lidar-captured 3D point cloud and a pseudo 3D point cloud predicted by surround-view cameras, resulting in better preservation of 3D geometric information. The feature fusion and further refinement operations are performed under the cylindrical

coordinate system. In FusionOcc [3], the authors proposed a cross-modality fusion module to generate a high-quality depth-aware visual feature, followed by a 2D to 3D view transformation, resulting in a depth-aware visual feature volumes under the Cartesian coordinate system. The lidar branch conducts voxelization and voxel encoding, resulting in a lidar feature volume also under the Cartesian coordinate system. Different modality feature volumes were fused via feature channel concatenation and further refined by a 3D Encoder. In DAOcc [5], the authors leverage multi-task learning to introduce an additional 3D supervision signal to guide intermediate features, leading to robust generalization and overall SOTA performance. Similarly, in Inverse++ [13], the authors leverage multi-task learning by incorporating an extra auxiliary 3D object detection branch. In addition, SDGOcc [6] incorporates a multi-task head to introduce a 2D semantic mask into the model training procedure, leveraging an additional 2D semantic mask to enhance the precision and densification of depth maps obtained from lidar point cloud projection, thereby boosting the model’s overall performance.

Despite achieving remarkable performance, these voxel-based methods incur redundant calculations for empty voxels, which are often dominant in 3D driving scenarios, resulting in inefficient computation. Our study presents a novel object-centric approach, aiming to address the aforementioned constraints by leveraging T-Primitives to model only occupied space in driving scenarios.

B. Object-Centric Modelling Approach

In the GaussianFormer series [14], [15], the authors proposed a 3D Gaussian-based object-centric modeling approach to improve computational efficiency. They further proposed a Gaussian-mixture model (GMM) to improve the model’s robustness. The 3D-to-3D Gaussian splatting operator, initially proposed in [16] for 3D-to-2D splatting, is further proposed

to boost the model's efficiency. In QuadricFormer [17], the authors proposed leveraging a superquadric primitive combined with a Gaussian probability kernel to achieve object-centric modeling and benefit from the geometric shape representation's flexibility, thereby improving model performance. In GaussianFormer3D [8], the authors extend the GaussianFormer work into a multi-sensor fusion scenario. By utilizing a set of 3D Gaussian primitives as an intermediate feature representation, the authors designed a pipeline that enables each 3D Gaussian primitive to aggregate features from different modalities and fuse them to perform 3D primitive-to-3D voxel volume Gaussian splatting. Benefiting from the object-centric modeling technique and multi-modal fusion, the model achieves significant performance and efficiency improvements. In GaussianFusionOcc [9], the authors proposed a GaussianFusionBlock module that performs efficient and high-quality feature aggregation and fusion across different modalities, allowing high-quality 3D Gaussian primitive modeling and leading to SOTA performance.

Though our proposed approach belongs to the object-centric modeling category, the key difference of our work compared to previous ones is that we explored Student's t-distribution and T-mixture model to enhance the model robustness. Furthermore, we proposed a multi-stage feature fusion pipeline to mitigate the drawbacks of each modality, resulting in better fused features. Lastly, we enhanced the primitive's geometric flexibility to provide a better intermediate representation, thereby achieving SOTA performance.

III. TFUSIONOCC

This work leverages a set of Student-T-distribution-based primitives combined with a 3D to 3D splatting operation to generate a dense 3D semantic occupancy grid of the surrounding scene by integrating information from surround-view cameras and lidar. Thus, the problem can be formulated as follows:

$$P_{refined}^T = F(Cam^1, Cam^2, \dots, Cam^N, Lidar, P^T) \quad (1)$$

$$Occ = Splat(P_{refined}^T) \quad (2)$$

where F refers to a multi-sensor fusion framework, P^T refers to a set of primitives based on T-distribution $P^T = \{p_1^T, p_2^T, \dots, p_K^T\}$, along with a set of query vectors $Q = \{q_1, q_2, \dots, q_K\}$, $P_{refined}^T$ refers to a set of T-distribution-based primitives refined through multi-sensor fusion framework, N refers to the total number of surround-view images and $Splat(\cdot)$ refers to the splatting operation. In the final predicted 3D semantic occupancy $Occ \in R^{\{X \times Y \times Z\}}$, each grid is assigned a semantic property ranging from 0 to C , where C refers to the total amount of semantic classes. In our case, a class value of 0 corresponds to an empty grid.

A. Overview

The overall architecture is shown in Figure 2. For the camera branch, given $\{img^1, img^2, \dots, img^N\}$ surround-view images, a 2D encoder and a decoder are leveraged to extract $V^{Cam} = \left\{ \left\{ V_n^l \right\}_{n=1}^N \in \mathbb{R}^{C \times H_l \times W_l} \right\}_{l=1}^L$ multi-scale

visual features. Meanwhile, a DepthNet is leveraged, resulting in a camera-based pseudo 3D point cloud P^{Cam} and a multi-scale camera-based dense depth maps $V_{depth}^{Cam} = \left\{ \left\{ V_{depth_n}^l \right\}_{n=1}^N \in \mathbb{R}^{D \times H_l \times W_l} \right\}_{l=1}^L$, where D refers to the total amount of depth-bins. The pseudo 3D point cloud P^{Cam} is further divided into cylindrical voxels, resulting in a camera-based 3D voxel volume Vol_{Cylin}^{Cam} defined in cylindrical coordinates. For the lidar branch, given a 3D point cloud P^{Lidar} from lidar, the cylindrical partition is first applied, resulting in a lidar-based 3D voxel volume Vol_{Cylin}^{Lidar} . Then a 3D encoder (e.g., Cylinder3D [18]) is used to extract lidar features V^{Lidar} in cylindrical coordinates. Meanwhile, P^{Lidar} is projected onto each surround-view camera frame, resulting in sparse multi-scale lidar-based depth maps $V_{depth}^{Lidar} = \left\{ \left\{ V_{depth_n}^l \right\}_{n=1}^N \in \mathbb{R}^{D \times H_l \times W_l} \right\}_{l=1}^L$. Then, a multi-stage feature fusion strategy is adopted. For the camera branch side, $V_{depth}^{Cam} \oplus V_{depth}^{Lidar}$ results in multi-scale fused dense depth maps V_{depth}^{fuse} . Then V_{depth}^{fuse} is encoded by a multi-layer perceptron (MLP) and added to V^{Cam} , resulting in multi-scale depth-aware visual features F^{Cam} . In addition, an outer product operation $F^{Cam} \otimes V_{depth}^{fuse}$ is conducted, resulting in a multi-scale lifted depth-aware visual feature Vol_{depth}^{Cam} . For the lidar branch side, each occupied voxel center of Vol_{Cylin}^{Lidar} serves as an anchor to project onto V^{Cam} , thereby aggregating semantic information. The aggregated semantic information is further fused with the lidar feature Vol_{Cylin}^{Lidar} through an early-fusion module, resulting in a semantic-aware lidar feature Vol_{sem}^{Lidar} . The projection operation begins with a transition from a cylindrical coordinate system to a Cartesian coordinate system, followed by a transition to a new coordinate frame. The Vol_{Cylin}^{Cam} and Vol_{Cylin}^{Lidar} are fused through the skeleton merge module, resulting in a fused voxel volume Vol_{Cylin}^{Fused} under cylindrical coordinates. The Vol_{Cylin}^{Fused} is then used as primitive anchors to initialize T-Primitives P^T under cylindrical coordinates. The P^T , Vol_{depth}^{Cam} and Vol_{sem}^{Lidar} are fed to the transformer module, which stacks the $N \times$ blocks to obtain a set of refined T-Primitives. Lastly, the refined set of T-Primitives performs a splatting operation, resulting in the final 3D semantic occupancy grid.

B. Image 2D Encoder and Decoder for Surround-View Images

The purpose of the image encoder is to capture both the spatial and semantic features of the surround-view images. These features serve as the foundation for the subsequent feature fusion procedure, and lastly, the task of 3D semantic occupancy prediction. In our approach, we first use a 2D backbone network (e.g. ResNet50 [19]) to extract visual features at multiple scales $V_{Encode}^{Cam} = \left\{ \left\{ V_n^l \right\}_{n=1}^N \in \mathbb{R}^{C_l \times H_l \times W_l} \right\}_{l=1}^L$. Subsequently, these features are fused using feature-pyramid networks (FPN), resulting in visual features $V^{Cam} = \left\{ \left\{ V_n^l \right\}_{n=1}^N \in \mathbb{R}^{C \times H_l \times W_l} \right\}_{l=1}^L$ that have the same feature channel dimension and resolutions that are $\frac{1}{8}$, $\frac{1}{16}$, and $\frac{1}{32}$ of the input image resolution, respectively. The deeper visual feature, with a smaller resolution, contains more semantic

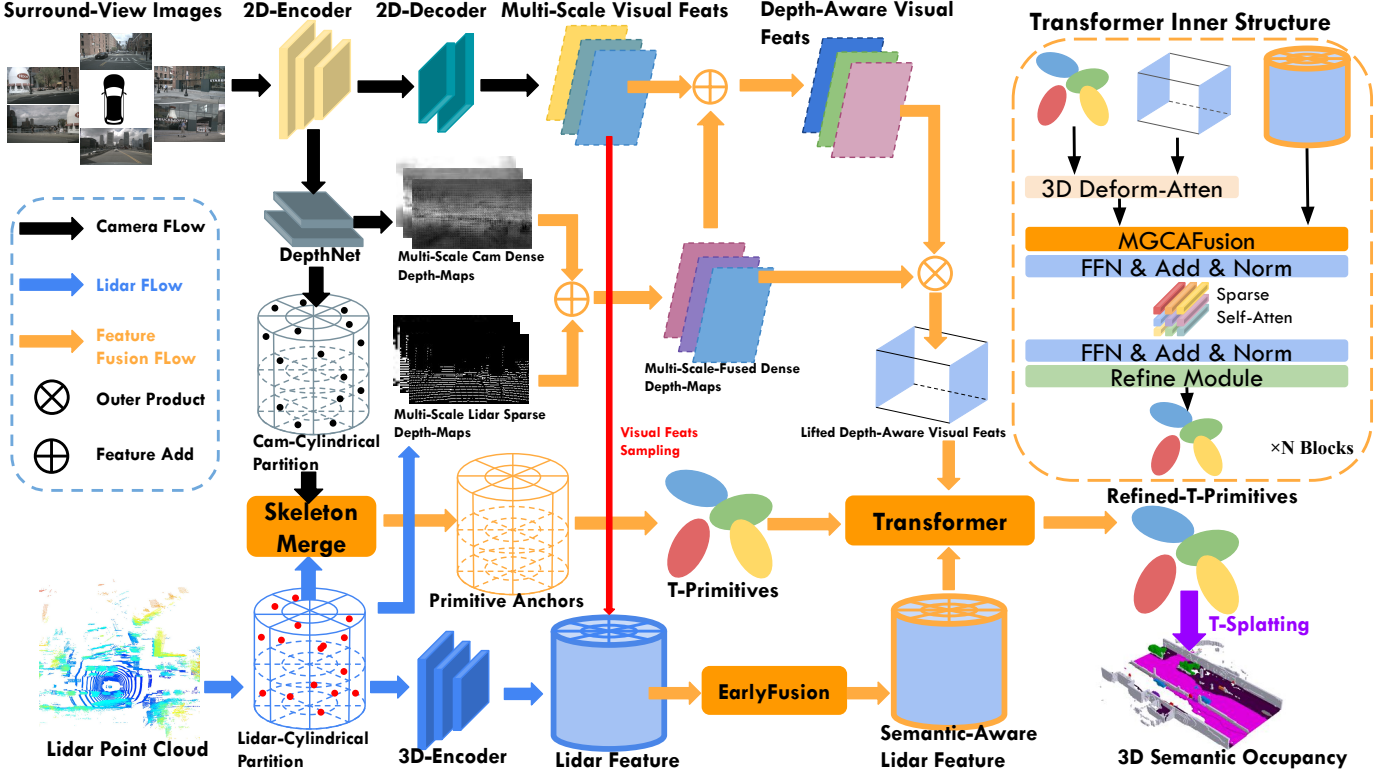


Fig. 2: **Overall architecture of TFusionOcc.** The pipeline comprises two different modality branches and a multi-stage feature fusion branch. The camera branch extracts multi-scale visual features and predicts a pseudo 3D point cloud from surround-view images. The pseudo 3D point cloud is further projected and cylindrically partitioned, resulting in camera-based, multi-scale, dense depth maps and a voxel volume defined under cylindrical coordinates. The lidar branch applies a cylindrical partition followed by a 3D encoder to extract the lidar feature. Meanwhile, the lidar point cloud is also projected to generate lidar-based, multi-scale, sparse depth maps. The feature fusion branch adopts a multi-stage fusion strategy to merge all outputs from the two-modality branch and leverages a proposed transformer to refine the T-primitives property through fused features.

information. In contrast, the relatively shallower visual feature, with larger resolutions, provides richer spatial details.

C. Camera-based Pseudo 3D Point Cloud and Multi-Scale Cam Dense Depth Maps Generation

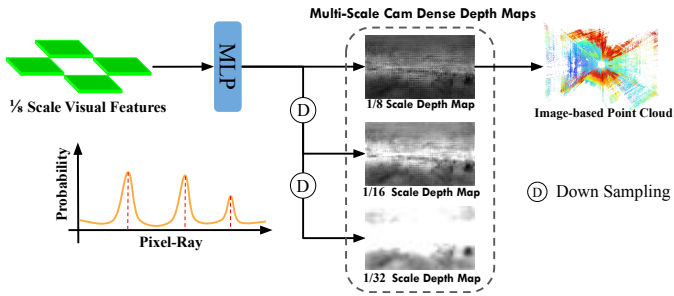


Fig. 3: **Inner Structure of DepthNet.** The 1/8-scale visual features are first used to generate a 1/8-scale depth map. Then, bilinear interpolation is leveraged to generate 1/16- and 1/32-scale depth maps. Meanwhile, the image-based pseudo-point cloud is generated solely from a 1/8-scale depth map.

The pseudo 3D point cloud P_{t}^{cam} and camera-based multi-scale dense depth maps V_{depth}^{cam} are generated through the DepthNet module as shown in Figure 3. The DepthNet module takes V_{Encode}^{Cam} as input and leverages a SECONDFPN [20] to

generate a single-scale visual feature $V_{sec}^{cam} = \{V_n\}_{n=1}^N \in \mathbb{R}^{C \times H_l \times W_l}$, whose resolution is $\frac{1}{8}$ of the input image. The V_{sec}^{cam} is further passed to an MLP to estimate the ray depth per-pixel, resulting in a single-scale depth map $V_{depth_n} \in \mathbb{R}^{N \times D \times H_l \times W_l}$. Bilinear interpolation with a 0.5 down sampling factor is applied iteratively to V_{depth_n} , resulting in two additional depth maps that have $\frac{1}{16}$ and $\frac{1}{32}$ resolution of the input image. Instead of performing depth estimation on each scale visual feature, our approach saves a certain amount of computation overhead while still maintaining a relatively high depth estimation precision. The predicted depth map and the two extra downsampled depth maps form $V_{depth}^{cam} = \left\{ \left\{ V_{depth_n}^l \right\}_{n=1}^N \in \mathbb{R}^{D \times H_l \times W_l} \right\}_{l=1}^{L=3}$. Meanwhile, the pseudo 3D point cloud P_{t}^{cam} is acquired only from $\frac{1}{8}$ scale depth map V_{depth_n} . Each pixel ray has a set of depth bins separated by 0.5m intervals. We followed the approach proposed in [15] to use 3D semantic occupancy annotations to supervise depth estimation. For each pixel ray, we take the highest probability depth bins of K to form P_{t}^{cam} .

D. Skeleton Merge Module

The primitive anchor initialization process is shown in Figure 4. Given the pseudo 3D point cloud derived from the camera P_{t}^{cam} and the real 3D point cloud of the lidar

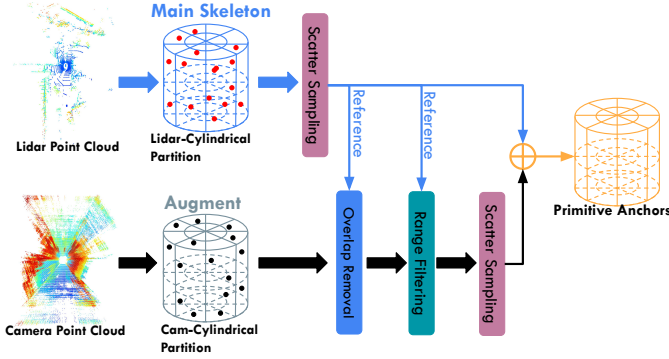


Fig. 4: **Skeleton Merge Module.** The upper lidar-branch serves as the main skeleton to provide a foundation structure for the 3D scene, and the bottom camera-branch serves as an augmentation based on the main skeleton to provide more detailed local structure to compensate for the fine-grained geometry of the main skeleton.

Pt^{lidar} , we first apply the cylindrical partition to both point clouds, resulting in two volumes of voxels Vol_{Cylin}^{Cam} and Vol_{Cylin}^{Lidar} under cylindrical coordinates. We then predefine the total primitive anchors of $M + N$, where the anchors M are sampled from Vol_{Cylin}^{Lidar} and the anchors N are sampled from Vol_{Cylin}^{Cam} , with a ratio of $M : N = 3 : 1$. Following [15], [21], we adopt the farthest point sampling strategy to obtain M Lidar anchors from Vol_{Cylin}^{Lidar} , which act as the main structural skeleton. Using these Lidar anchors as reference, any voxel in Vol_{Cylin}^{Cam} that spatially overlaps with the LiDAR anchors is removed. In addition, we impose a radius constraint $r = 5\text{m}$ to perform range filtering. Any voxel in Vol_{Cylin}^{Cam} whose closest Lidar anchor is farther away than r is also discarded. Then, N Camera anchors are obtained using the farthest point sampling strategy on the remaining voxels in Vol_{Cylin}^{Cam} . Based on the aforementioned filtering and sampling strategy, we acquire a final set of $M + N$ anchors whose locations will be used to initialize a set of T-primitives.

The skeleton merge module takes advantage of the lidar strength in preserving the fine-grained 3D geometry of the scene and takes advantage of its Vol_{Cylin}^{Lidar} to extract the main skeleton. Meanwhile, the module also leverages the camera's strength in handling occlusion scenes and uses its Vol_{Cylin}^{Cam} to extract the augmented skeleton surrounding the main skeleton. The fused skeleton preserves the finer-grained 3D geometry of the scene by combining the advantages of both modalities.

E. Multi-scale-Fused Dense Depth-Maps Generation

Given multi-scale camera dense depth maps V_{depth}^{cam} and multi-scale lidar sparse depth maps V_{depth}^{lidar} , we first go through per-pixel level value addition followed by a value clamp, resulting in the final multi-scale fused dense depth maps as shown in Figure 5 upper. The detail of the addition of the per-pixel ray value is shown in Figure 5 bottom. For the camera side, each pixel ray has D number of depth bins, and the interval between each depth bin is 0.5m . The DepthNet predicts the probability that each depth bin being occupied with a value in the range of $[0, 1]$. On the lidar side, each pixel ray also has D depth bins, but only one depth bin has

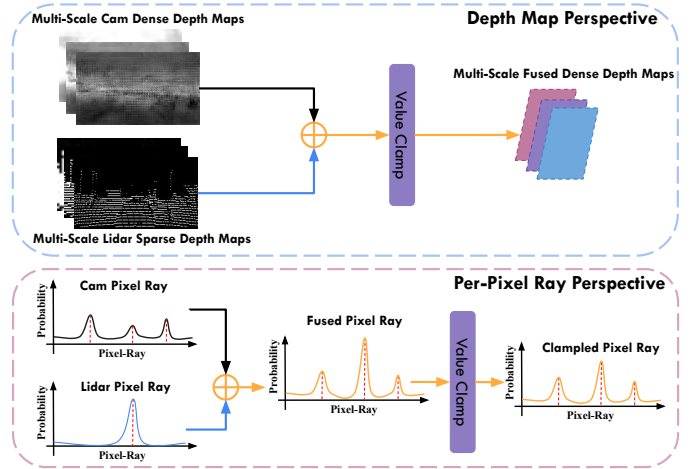


Fig. 5: **Multi-Scale Fused Dense Depth Maps Generation.** The upper part exhibits general multi-modality depth map fusion from a depth map perspective, and the bottom part demonstrates the detailed multi-modality depth map fusion from a per-pixel ray perspective.

been assigned a probability value of 1.0, while all other depth bins are assigned a probability value of 0. When adding the camera pixel ray to the lidar pixel ray, the resulting fused pixel ray may have some depth-bin probability values exceeding 1.0; therefore, these values need to be clamped within the range $[0, 1]$.

This multi-modality depth map fusion, on the one hand, solves the sparsity problem of lidar-based depth maps, and on the other hand, mitigates the inaccurate depth estimation problem of camera-based depth maps, resulting in denser and highly precise fused depth maps.

F. Early-Fusion Module

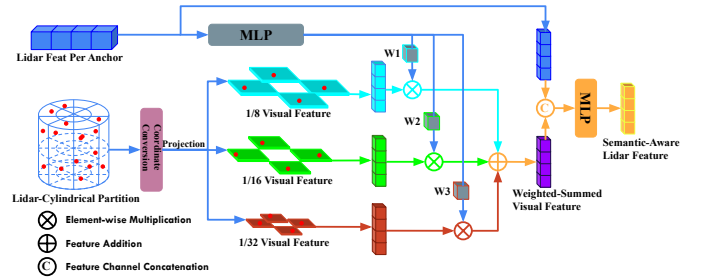


Fig. 6: **Early-Fusion Module.** Each occupied voxel centre in Vol_{Cylin}^{Lidar} serves as an anchor and is projected onto multi-scale visual features to aggregate semantic information, yielding a semantic-aware lidar feature.

The detailed inner structure of the Early-Fusion module is shown in Figure 6. Given the sparse volume of the voxel Vol_{Cylin}^{Lidar} in cylindrical coordinates, we leverage each occupied voxel center as an anchor and convert each anchor position from cylindrical coordinates to Cartesian coordinates. Then, each anchor is projected onto multi-scale visual features V^{Cam} to aggregate semantic information at three scales. The aggregated three-scale visual features are weighted, summed, and concatenated back to the corresponding voxel feature, then fed

through an MLP layer to perform the feature fusion, resulting in the last semantic-aware lidar feature Vol_{sem}^{Lidar} .

G. T-Primitive Representation

Following the GaussianFormer [14], [15], [17] series, we propose the probabilistic Student's T-distribution superposition as an efficient and effective 3D scene representation. Specifically, we propose three types of primitives that are enhanced by the inner kernel of T-distribution or T-distribution-like. The first is the Student-T-distribution-based primitive, which has the property as follows:

$$P_i^T(m_i, s_i, r_i, \alpha_i, c_i) \quad (3)$$

where m_i , s_i , r_i , α_i and c_i refer to the mean, scale value for the x, y, z axes, quaternion vector, opacity and semantic vector of the i -th primitive, respectively. The second is the Student-T-distribution-based superquadric primitive, which has the property as follows:

$$P_{SQi}^T(m_i, s_i, r_i, \alpha_i, \epsilon_{1_i}, \epsilon_{2_i}, c_i) \quad (4)$$

where ϵ_1 and ϵ_2 are the shape exponents of the superquadric. The third is the Student-T-distribution-based superquadric with inverse-warp primitive that has the property as follows:

$$P_{SQIWi}^T(m_i, s_i, r_i, \alpha_i, \epsilon_{1_i}, \epsilon_{2_i}, w_i, c_i) \quad (5)$$

where w_i is the learnable weighting scalar valued between -1 and 1.

Similarly to [15], we decompose the 3D modeling target into geometry and semantics predictions, and adopt the multiplication theorem of probability and the T-mixture model to address them probabilistically, respectively. What is more, compared to the Gaussian mixture model, the T-mixture model significantly improves robustness against outliers.

1) *Student-T-Distribution Based Geometry Prediction*: To restrict T-Primitives to represent only occupied regions for geometry prediction, we interpret the T-distribution primitives $P^T = \{p_i^T\}_{i=1}^K$ as the probability of their surrounding space being occupied. In detail, we assign a probability value of 100% to the centers of the T-distribution, which decays with respect to the distance from the centers m :

$$\alpha(x; p_i^T) = \left[1 + \frac{1}{\nu} (x - m)^T \Sigma^{-1} (x - m) \right]^{-\frac{\nu+3}{2}} \quad (6)$$

where ν refers to the degree of freedom, it is obtained by calculating how many voxels are intercepted by each T-primitive minus 1, and $\alpha(x; p_i^T)$ denotes the probability of the point x being occupied induced by the i -th T-primitive. Equation 6 assigns a high probability of occupancy when the point x is close to the center m of the i -th T-primitive, which prevents any T-primitive from describing an empty area. To further derive the overall probability of occupancy, we assume that the probabilities of a point being occupied by different T-primitives are mutually independent, and thus we can aggregate them according to the multiplication theorem of probability:

$$\alpha(x) = 1 - \prod_{i=1}^K (1 - \alpha(x; p_i^T)) \quad (7)$$

where $\alpha(x)$ represents the overall probability of occupancy at point x .

2) *T-Mixture Model Based Semantic Prediction*: In addition to the Student-T-distribution-based Geometry modeling, we also need to perform the Student-T-distribution-based semantics prediction. Following [15], we interpret the set of T-primitives as a T-mixture model, where the semantics prediction could be formulated as calculating the expectation of semantics given the probabilistic T-mixture model.

To be specific, we take the original opacity properties α as the prior distribution of the T-primitives, which is normalized by $l1$. Then, the T-primitive probabilistic distribution is adopted as a conditional probability. In addition, we normalize each T-primitive's original semantics properties c_i with a softmax activation function, yielding \tilde{c}_i to ensure the boundness of predicted semantics. Lastly, the expectation calculation of the T-mixture model can be formulated as:

$$e(x; P^T) = \sum_{i=1}^K p(P_i^T | x) \tilde{c}_i = \frac{\sum_{i=1}^K p(x | P_i^T) a_i \tilde{c}_i}{\sum_{j=1}^K p(x | P_j^T) a_j} \quad (8)$$

where $p(P_i^T | x)$, $p(x | P_i^T)$ and \tilde{c}_i denote the posterior probability of point x belonging to the i -th T-primitive distribution, the conditional probability of point x given the i -th T-primitive distribution, and the softmax-normalized semantic properties, respectively.

Lastly, based on the geometry and semantic predictions, we combine the two prediction results together, resulting in the final 3D semantic occupancy prediction. The combination process is formulated as follows.

$$Occ = [1 - \alpha(x); \alpha(x) \cdot e(x; P^T)] \quad (9)$$

where $1 - \alpha(x)$ refers to the probability of the empty class and $\alpha(x) \cdot e(x; P^T)$ refers to the final semantic probabilities. The $\alpha(x)$ is used to weight the initial semantic prediction.

3) *Student-T-Distribution Based Primitive*: The straightforward T-distribution primitive $p(x | P_i^T)$ can be formulated as:

$$p(x | P_i^T) = \frac{\Gamma(\frac{\nu+3}{2})}{\Gamma(\frac{\nu}{2}) \cdot (\nu\pi)^{3/2} \cdot |\Sigma|^{1/2}} \cdot \left[1 + \frac{1}{\nu} (x - m)^T \Sigma^{-1} (x - m) \right]^{-\frac{\nu+3}{2}} \quad (10)$$

where ν refers to the degree of freedom, the same as in Equation 6, it is obtained by calculating how many voxels are intercepted by each T-primitive minus 1. Γ refers to the gamma function, and performs the $\Gamma(n) = (n-1)!$ operation. Compared to Gaussian-primitive, this T-primitive is highly tailed in its probability distribution, leading to better robustness against outliers.

4) *Student-T-Distribution Based SuperQuadric Primitive*: Following the quadricformer [17], we use the T-probabilistic modeling mechanism to convert superquadrics into occupancy probabilities. We first transform the 3D point position (X, Y, Z) , which is occupied by the T-Superquadric primitive, into its local coordinate system as:

$$\begin{bmatrix} X_S \\ Y_S \\ Z_S \end{bmatrix} = R \times \begin{bmatrix} X - m_x \\ Y - m_y \\ Z - m_z \end{bmatrix} \quad (11)$$

where (X_S, Y_S, Z_S) refers to the local coordinate under the T-Superquadric primitive, and R is the rotation matrix of each T-Superquadric primitive. Then, the occupancy probability of the 3D point (X, Y, Z) associated with each T-Superquadric primitive can be computed as:

$$f(X_S, Y_S, Z_S) = \left(\left(\frac{X_S}{S_x} \right)^{\frac{2}{\epsilon_2}} + \left(\frac{Y_S}{S_y} \right)^{\frac{2}{\epsilon_2}} \right)^{\frac{\epsilon_2}{\epsilon_1}} + \left(\frac{Z_S}{S_z} \right)^{\frac{2}{\epsilon_1}} \quad (12)$$

$$p(x|P_{SQi}^T) = \left(1 + \frac{1}{\nu} \cdot f(X_S, Y_S, Z_S) \right)^{-\frac{\nu+3}{2}} \quad (13)$$

where (S_x, S_y, S_z) refers to the scale parameters along the X, Y, Z axes, ϵ_1 and ϵ_2 are the shape exponents of the superquadric.

5) *Student-T-Distribution Based SuperQuadric With Inverse-Warp Primitive*: So far, thanks to the T-distribution kernel enhancement, the T-Superquadric primitive is robust to outliers. Nevertheless, the T-Superquadric primitive has a very limited shape variety. It can only exhibit convex, symmetric shapes and cannot capture non-convex, asymmetric shapes, which are common in the daily 3D driving scene. To solve this limitation, we make the T-Superquadric primitive deformable through inverse-warp enhancement. Specifically, we choose 24 basis field functions $\{B_i(u, v, w)\}_{i=1}^{24}$, where u, v, w refers to three inputs, respectively, to deform the local coordinates (X_S, Y_S, Z_S) as follows:

$$u = \frac{X_S}{S_x}, v = \frac{Y_S}{S_y}, w = \frac{Z_S}{S_z} \quad (14)$$

$$\begin{bmatrix} \tilde{X}_S \\ \tilde{Y}_S \\ \tilde{Z}_S \end{bmatrix} = \begin{bmatrix} X_S \\ Y_S \\ Z_S \end{bmatrix} - \sum_{i=1}^{24} \omega_i \cdot B_i(u, v, w) \quad (15)$$

where ω_i is the learnable weighting scalar valued between -1 and 1. Then, the occupancy probability of the 3D point associated with each T-Superquadric-Inverse-Warp primitive can be calculated as follows:

$$f(\tilde{X}_S, \tilde{Y}_S, \tilde{Z}_S) = \left(\left(\frac{\tilde{X}_S}{S_x} \right)^{\frac{2}{\epsilon_2}} + \left(\frac{\tilde{Y}_S}{S_y} \right)^{\frac{2}{\epsilon_2}} \right)^{\frac{\epsilon_2}{\epsilon_1}} + \left(\frac{\tilde{Z}_S}{S_z} \right)^{\frac{2}{\epsilon_1}} \quad (16)$$

$$p(x|P_{SQIWi}^T) = \left(1 + \frac{1}{\nu} \cdot f(\tilde{X}_S, \tilde{Y}_S, \tilde{Z}_S) \right)^{-\frac{\nu+3}{2}} \quad (17)$$

Each basis field function is listed in Table I. B_1 to B_9 provide constants, linear, basic shears, and taper deformation. B_{10} to B_{18} enable full shear, twist, and bending deformation. Moreover, B_{19} to B_{24} provide quadratics, radial bulge, and smooth corner deformation.

H. Transformer

The general inner structure of the proposed transformer is shown in Figure 2. It takes a set of T-primitives, multi-scale lifted depth-aware visual features, and a semantic-aware lidar feature as input, and proceeds through a fused depth-map-guided 3D deformable attention module, a multi-gate cross-attention fusion module, two MLP-based feed-forward

Basis Field	u	v	w
B_1	1.0	0.0	0.0
B_2	0.0	1.0	0.0
B_3	0.0	0.0	1.0
B_4	u	0.0	0.0
B_5	0.0	v	0.0
B_6	0.0	0.0	w
B_7	v	0.0	0.0
B_8	w	0.0	0.0
B_9	0.0	w	0.0
B_{10}	0.0	u	0.0
B_{11}	0.0	0.0	u
B_{12}	0.0	0.0	v
B_{13}	$-w * v$	$w * u$	0.0
B_{14}	0.0	$-u * w$	$u * v$
B_{15}	$v * w$	0.0	$-v * u$
B_{16}	w^2	0.0	0.0
B_{17}	0.0	w^2	0.0
B_{18}	u^2	0.0	$u^2 + v^2$
B_{19}	0.0	v^2	0.0
B_{20}	0.0	0.0	w^2
B_{21}	0.0	0.0	0.0
B_{22}	$(u^2 + v^2) * u$	$(u^2 + v^2) * v$	0.0
B_{23}	$u * v$	$u * v$	0.0
B_{24}	$u * v^2$	$u^2 * v$	0.0

TABLE I: The 24 basis field functions make the T-Superquadric deformable. Those functions enable full shears, twists, bends, quadratics, radial bulge and smooth corners.

modules, a 3D sparse convolution-based self-attention module, and a T-primitive properties refine module iteratively N times, resulting in the last refined T-primitives. The following sections will introduce the key implementation details of each module.

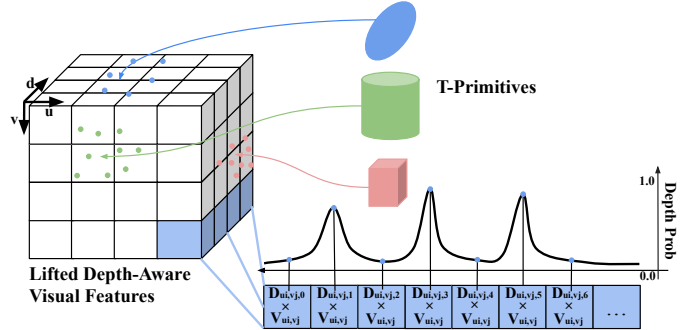


Fig. 7: **3D Deformable Attention** For the same visual feature at location (u_i, v_j) , several different depth values ranging between $[0, 1.0]$ along the depth-axis are used to weight the same pixel feature, resulting in the depth encoded visual feature to mitigate the projection ambiguity problem stemming from the projection process.

1) Fused Depth Map based 3D Deformable Attention:

Taking multi-scale lifted depth-aware visual features and a set of T-primitive as input, we use a 3D deformable attention operator, namely DFA3D [22], which performs feature aggregation on lifted visual features to mitigate the 3D to 2D projection ambiguity problem, to aggregate visual features for each T-primitive. As shown in Figure 2 camera branch and Figure 7, the multi-scale lifted depth-aware visual features Vol_{depth}^{Cam} are obtained through outer product operation $F_{depth}^{Cam} \otimes V_{depth}^{fuse}$,

this operation gives an accurate depth encoding for each visual feature in the feature map. For each T-primitive feature sampling p_i^T , we first use the mean location m_i of each p_i^T as the center, convert the center location from the cylindrical coordinate to the cartesian coordinate, and feed its associate query feature q_i to an MLP layer, resulting in 13 offsets Δm_j with respect to the center to form a set of 3D sampling points $m_i^{samp} = \{m_i^{samp} = m_i + \Delta m_j \mid j = 1, \dots, 13\}$. Then, we leverage extrinsic and intrinsic matrices to project each 3D sampling point m_i^{samp} onto the lifted depth-aware visual features, resulting in the location of the sampling of the pixel frame $\bar{m}_i^{samp} = (u_i, v_i, d_i)$. Lastly, a 3D deformable attention operator DFA3D takes \bar{m}_i^{samp} as a sampling location to perform cross-attention visual feature aggregation on Vol_{depth}^{Cam} , resulting in an updated query feature $q_i^{updated}$. The overall sampling process can be formulated as follows:

$$q_i^{updated} = \sum_{i=1}^{13} DFA3D(q_i, \bar{m}_i^{samp}, Vol_{depth}^{Cam}) \quad (18)$$

After the 3D cross-attention process, $q_i^{updated}$ already aggregates sufficient depth-aware visual features and is passed to the MGCAFusion module for feature fusion. Meanwhile, the set of 3D sampling points m_i^{samp} for each T-primitive is also passed on to the MGCAFusion module for semantic-aware lidar feature aggregation.

2) *Multi-Gate Cross-Attention Fusion (MGCAFusion) Module:* Given a set of 3D sampling points m_i^{samp} for each T-primitive, we apply bilinear interpolation on Vol_{sem}^{Lidar} to aggregate a semantic-aware lidar feature for each T-primitive. The detailed implementation of the multi-gate cross attention fusion module (MGCAFusion) is demonstrated in Figure 8. It consists of two central parts, the weighted summation fusion part, as highlighted in the green rectangle on the left of Figure 8 and the gated concatenation fusion part, as highlighted in the pink rectangle on the right of Figure 8. Both parts take the same inputs, but perform different feature fusion strategies.

For the weighted summation fusion part, the semantic-aware lidar feature and the depth-aware visual feature are summed in elements first, then passed through an MLP layer followed by a softmax layer, resulting in two weight values, W_{Lidar} and W_{Vis} . The W_{Lidar} and W_{Vis} are multiplied again with the corresponding semantic-aware lidar feature and depth-aware visual feature, respectively, resulting in the weighted lidar feature and the weighted visual feature. Lastly, the weighted lidar feature and the weighted visual feature are summed and passed through an MLP layer, yielding the summation fusion feature.

For the gated concatenation fusion part, the semantic-aware lidar feature and the depth-aware visual feature are passed through an MLP layer, followed by a sigmoid function, respectively, resulting in a visual gate vector G_{Vis} and a lidar gate vector G_{Lidar} . G_{Vis} is element-wise multiplied with the semantic-aware lidar feature, followed by a skip connection that results in the gated lidar feature. G_{Lidar} is element-wise multiplied with the depth-aware visual feature, followed by a skip connection that results in the gated visual feature. The gated Lidar

and visual features are concatenated along the feature channel dimension, followed by an MLP layer that reduces the fused feature channel dimension, yielding the concatenation fusion feature.

Lastly, the summation and concatenation fusion features are combined via feature-channel concatenation, followed by an MLP layer, yielding the final fused feature.

3) *3D Sparse Conv-based Self-Attention Module:* The self-attention module is demonstrated in Figure 9. Each T-primitive center m_i is treated as a 3D point, and we can acquire a set of 3D points based on T-primitive. Then, this T-primitive-based sparse 3D point cloud undergoes a coordinate transformation from Cartesian to cylindrical coordinates, followed by voxelization, yielding a sparse voxel volume in cylindrical coordinates. Lastly, the 3D sparse convolution applies to this sparse voxel volume to perform the self-attention operation. Since our T-primitives are initialized in cylindrical coordinates, we perform the self-attention operation in the same coordinates to better preserve the scene’s fine-grained 3D geometry.

4) *T-Primitive Property Refinement Module:* Since T-primitive queries have aggregated sufficient semantic and 3D geometry information in the previous 3D deformable attention, self-attention, and MGCAFusion modules, we use each query vector to update its associated T-primitive properties. Specifically, for three types of T-primitives, we feed each type of T-primitive query to an MLP layer to obtain the intermediate properties, and we combine the intermediate properties with the initial properties to achieve the refinement of the T-primitive property. The property refinement details for three types of T-primitives are formulated as:

$$\begin{aligned} MLP(Q_{P_i}) &\Rightarrow (\hat{m}_i, \hat{s}_i, \hat{r}_i, \hat{c}_i) \\ MLP(Q_{SQ_i}) &\Rightarrow (\hat{m}_i, \hat{s}_i, \hat{r}_i, \hat{\epsilon}_{1i}, \hat{\epsilon}_{2i}, \hat{c}_i) \\ MLP(Q_{SQIW_i}) &\Rightarrow (\hat{m}_i, \hat{s}_i, \hat{r}_i, \hat{\epsilon}_{1i}, \hat{\epsilon}_{2i}, \hat{w}_i, \hat{c}_i) \\ P_{New_i}^T &= (m + \hat{m}_i, \hat{s}_i, \hat{r}_i, \hat{c}_i) \\ P_{New_{SQ_i}}^T &= (m + \hat{m}_i, \hat{s}_i, \hat{r}_i, \hat{\epsilon}_{1i}, \hat{\epsilon}_{2i}, \hat{c}_i) \\ P_{New_{SQIW_i}}^T &= (m + \hat{m}_i, \hat{s}_i, \hat{r}_i, \hat{\epsilon}_{1i}, \hat{\epsilon}_{2i}, \hat{w}_i, \hat{c}_i) \end{aligned} \quad (19)$$

IV. EXPERIMENTAL RESULTS

A. Implementation Details

The TFusionOcc model takes six surround-view images and 10 lidar sweeps per data sample and leverages ResNet50-DCN [19] as a 2D Backbone, initialized with weights from FCOS3D [23]. The transformer layer is stacked four times iteratively. AdamW optimizer is used, with an initial learning rate of 2e-4 and a weight decay of 0.01. The learning rate is decayed using a multistep scheduler. The predicted occupancy has a resolution of $200 \times 200 \times 16$ for full-scale evaluation on nuScenes-Surroundocc, nuScenes-Occ3D and nuScenes-C datasets. For data augmentation, we employ photometric distortions and a grid mask to the input images during training. Model training is conducted on two H100 GPUs with 94GB of memory.

B. Loss Function

To train TFusionOcc, we take advantage of the Lovász-Softmax loss [24] L_{lovasz} and the binary cross-entropy loss

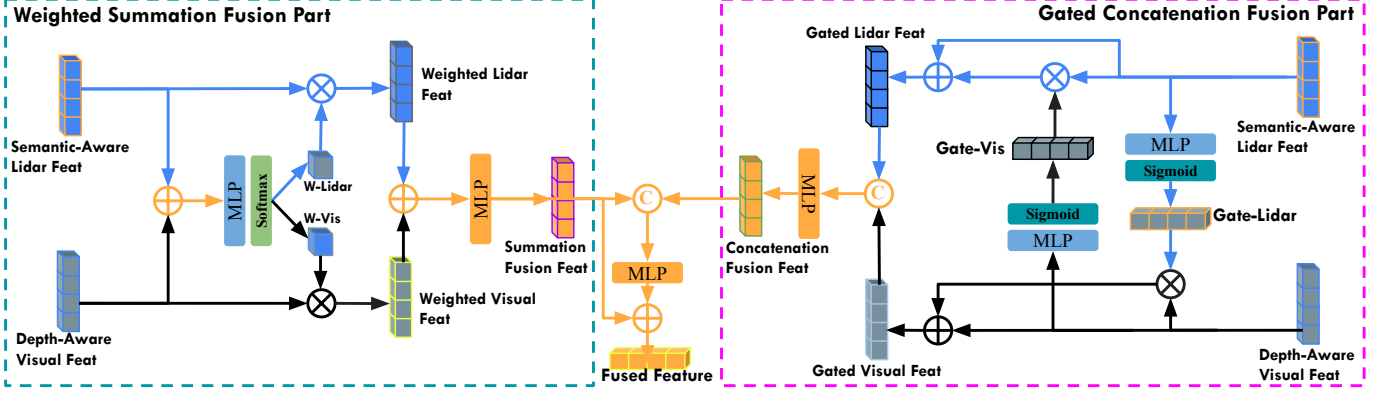


Fig. 8: **Multi-Gate Cross Attention Fusion Module.** The left part exhibits the multi-modality weighted summation fusion part, and the right part exhibits the multi-modality gated concatenation fusion part. The outputs of the two major parts are further fused to produce the final fused feature.

Self-Attention Pipeline

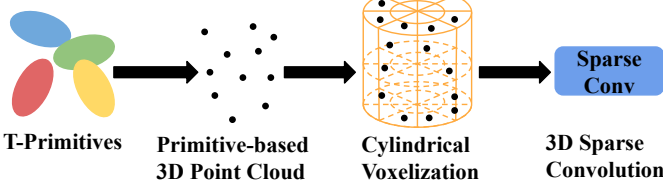


Fig. 9: **Sparse-Convolution-Based Self-Attention Pipeline.** The center of T-primitives is treated as a 3D point to form a primitive-based 3D point cloud. We apply a cylindrical partition to the obtained 3D point cloud, followed by a 3D sparse convolution to realise self-attention.

L_{BCE} to optimize the 3D semantic occupancy task. For depth supervision, a binary cross-entropy loss L_{BCE}^{depth} is used to refine the depth distribution feature. The final loss is formulated as follows.

$$L_{Total} = L_{lovasz} + \lambda \cdot L_{BCE} + L_{BCE}^{depth} \quad (20)$$

where λ balance the loss weight, in our case, we set $\lambda = 10$. The final loss is applied only to the output of the last iterated transformer.

C. Dataset

The public nuScenes dataset [10], specifically designed for autonomous driving purposes, serves as the primary data source for our experiments. Furthermore, nuScenes-C [11], which not only augments the existing nuScenes dataset with additional simulated challenging scenarios, such as snow, fog, lowlight and brightness, etc, but also simulates several engineering failure cases, such as frame lost and camera crash, etc, is employed as a supplementary dataset to further evaluate the robustness of the proposed algorithm. Each corruption scenario in nuScenes-C has three severities, ranked easy, mid, and hard, respectively.

To perform the 3D semantic occupancy prediction task, we use dense labels obtained from SurroundOcc [25] and Occ3D [26], respectively. Since the test set lacks semantic labels, we train our model on the training set and evaluate its performance

using the validation set. For annotations from SurroundOcc, we set the range of the X and Y axes to $[-50, 50]$ meters and the Z axis to $[-5, 3]$ meters under lidar coordinates. For annotations from Occ3D, we set the range of the X and Y axes to $[-40, 40]$ meters and the Z axis to $[-1, 5.4]$ meters under the ego coordinates. The input images have a resolution of 1600×900 pixels, while the final output of the semantic occupancy prediction branch is represented with a resolution of $200 \times 200 \times 16$. The annotations from SurroundOcc contain a total of 17 semantic classes, while the annotations from Occ3D comprise 18 semantic classes. Label 0 refers to free voxels in both annotations.

Additionally, following the methodology proposed in [1], we conduct an in-depth analysis of our model performance in challenging scenarios, specifically in rainy and night conditions. This evaluation is carried out using the annotation file provided by [1].

D. Performance Evaluate Metrics

To assess the performance of various SOTA algorithms and compare them with our approach in the 3D semantic occupancy prediction task, we utilize the intersection over union (IoU) to evaluate each semantic class. Moreover, we employ the mean IoU over all semantic classes (mIoU) as a comprehensive evaluation metric:

$$IoU = \frac{TP}{TP + FP + FN} \quad (21)$$

and

$$mIoU = \frac{1}{Clz} \sum_{i=1}^{Clz} \frac{TP_i}{TP_i + FP_i + FN_i} \quad (22)$$

where TP , FP , and FN represent the counts of true positives, false positives, and false negatives in our predictions, respectively, while Clz denotes the total class number.

E. Model Performance Analysis

To demonstrate the performance of our proposed TFusionOcc, we evaluated it on the Surroundocc-nuScenes and

Occ3D-nuScenes benchmarks. For each benchmark, we evaluate our model across three primitive settings, including T-P (general T-primitive), T-SQ (T-superquadric), and T-SQ-IW (deformable T-superquadric or T-superquadric with inverse-warp), with 12800 and 25600 total primitives, respectively. The results of the experiment on the surroundocc-nuScenes and Occ3D-nuScenes benchmarks are shown in Table II and Table III, respectively.

In both benchmarks, TFusionOcc (T-SQ-IW) settings achieve the best and second-best performance, demonstrating the importance of the primitives' shape variety and robustness. Specifically, our proposed method excels at detecting background objects, including drivable surfaces, other flat areas, sidewalks, terrain, man-made structures, and vegetation. In addition, our model performs significantly well on relatively small foreground objects, such as barriers, bicycles, cars, motorcycles, pedestrians, and traffic cones.

Our method, which only adopts a single 3D supervision signal, achieved par-performance in comparison with algorithms that leverage multi-task learning to receive dual supervision signals, such as DAOcc [5] in the Surroundocc-nuScenes benchmark that incorporates a 3D object detection head and a 3D semantic occupancy prediction head during training, and SDGOcc [6] in the Occ3D-nuScenes benchmark, which incorporates a 2D semantic segmentation head and a 3D semantic occupancy prediction head during training.

F. Challenging Scenarios Performance Analysis

To further examine the performance and robustness of the proposed algorithm, we follow [1] to evaluate TFusionOcc with different T-primitive representations under challenging rainy and night-time scenarios and the experiment results are shown in Table IV and Table V, respectively.

In the rainy scenario, raindrops on the camera lens cause focus blur and degrade the quality of semantic information provided by the camera branch. Furthermore, laser beam reflections during rainy conditions degraded the quality of the geometry information provided by the lidar branch. As a result, all algorithms in the benchmark exhibit varying degrees of performance degradation. However, our proposed method benefits from a multi-stage feature fusion design and the flexible T-Primitive representation, exhibits the least performance degradation in the benchmark, demonstrating high robustness against challenging rainy conditions.

In the nighttime scenario, due to the nature of the camera sensor, which is sensitive to the ambient lightning conditions, the dim lighting condition during the nighttime leads to semantic information loss in the camera branch. Meanwhile, the depth-estimation accuracy from the camera branch drops. As a result, all algorithms in the benchmark experience severe performance degradation around 1.56% to 11.10% under the IoU metric and 8.89% to 12.50% under the mIoU metric. Among all performance degradation algorithms, our method still achieves SOTA performance, demonstrating superior feature fusion and information filtering capabilities.

G. Performance Analysis On nuScenes-C Dataset

To further assess the robustness of the proposed algorithm in extreme conditions, such as snow, fog, and sensor malfunctions, we use the nuScenes-C dataset and evaluate TFusionOcc at different levels of corruption and severity. The results of the experiment for several camera corruption settings are shown in Tables VI, VII, and X, and the results for several lidar corruption settings are shown in Tables VIII, IX, and XI. Note that since the nuScenes-C dataset only provides single-lidar-sweep corruption data, and our model leverages 10 lidar sweeps. Hence, when evaluating our model across different lidar corruption settings, we use only a single corrupted lidar sweep from the nuScenes-C dataset, and the model performance under the clean setting differs from that in Table II due to a much sparser lidar point cloud. In the camera corruption scenario, our model shows strong robustness against camera crashes, frame loss, brightness, and fog, as measured by the mIoU metric. Nevertheless, the motion blur and snow scenarios cause significant performance degradation in our model. With around 5.04% to 8.43% and 4.91% to 6.64% degradation under the IoU metric, 10.00% to 10.63% and 14.02% to 14.55% degradation under the mIoU metric for the motion blur and snow corruption case, respectively. In the lidar corruption scenario, our model is sensitive to lidar point cloud density and quality degradation, demonstrating its firm reliance on lidar point cloud quality.

H. Performance Analysis On Varying Distance

1) Performance Variation Trend At Different Distances.:

Following [1], we take the ego vehicle as the origin and R as the radius. By adjusting the length of R , we evaluate our proposed method against other SOTA algorithms at varying perception distance radius [20m, 25m, 30m, 35m, 40m, 45m, 50m], including challenging rainy and night scenarios. The trend of performance variation is shown in Figure 10.

The trend of performance variation across the whole validation set, as shown in Figures 10a and 10d, aligns with the performance benchmark in Table II. In the rainy scenario, the performance variation trend of our proposed method is similar to the results of the whole validation set experiment, except that the performance gap between different T-Primitive settings further narrows down to 0.11% to 2.90% under the mIoU metric and 0.44% to 1.74% under the IoU metric due to the semantic and geometric information loss from both sensors. In the nighttime scenario, we discover that our T-SQ-25600 setting outperforms the second-best T-SQ-IW-12800 setting within a 35-meter perception range under the mIoU metric, as shown in Figure 10c. This phenomenon may stem from the fact that more primitives can better capture close-range details, leading to better robustness against challenging dim-lighting conditions.

2) Performance In Different Sectors Ranges: To thoroughly study the effect of distance on the proposed method, we further evaluate our TFusionOcc against other SOTA algorithms in different sector ranges [0~10m, 10~20m, 20~30m, 30~40m, 40~50m] and present the evaluation results in Figure 11.

Method	2D-Backbone	Modality	IoU	mIoU	others	barrier	bicycle	bus	car	const. veh.	motorcycle	pedestrian	traffic cone	trailer	truck	drive. surf.	other flat	sidewalk	terrain	manmade	vegetation
MonoScene [27]	R101-DCN	C	23.96	7.31	4.03	0.35	8.00	8.04	2.90	0.28	1.16	0.67	4.01	4.35	27.72	5.20	15.13	11.29	9.03	14.86	
Atlas [28]	-	C	28.66	15.00	10.64	5.68	19.66	24.94	8.90	8.84	6.47	3.28	10.42	16.21	34.86	15.46	21.89	20.95	11.21	20.54	
BEVFormer [29]	R101-DCN	C	30.50	16.75	14.22	6.58	23.46	28.28	8.66	10.77	6.64	4.05	11.20	17.78	37.28	18.00	22.88	22.17	13.80	22.21	
TPVFormer [30]	R101-DCN	C	30.86	17.10	15.96	5.31	23.86	27.32	9.79	8.74	7.09	5.20	10.97	19.22	38.87	21.25	24.26	23.15	11.73	20.81	
C-CONet [31]	R101	C	26.10	18.40	18.60	10.00	26.40	27.40	8.60	15.70	13.30	9.70	10.90	20.20	33.00	20.70	21.40	21.80	14.70	21.30	
InverseMatrixVT3D [32]	R101-DCN	C	30.03	18.88	18.39	12.46	26.30	29.11	11.00	15.74	14.78	11.38	13.31	21.61	36.30	19.97	21.26	20.43	11.49	18.47	
OccFormer [33]	R101-DCN	C	31.39	19.03	18.65	10.41	23.92	30.29	10.31	14.19	13.59	10.13	12.49	20.77	38.78	19.79	24.19	22.21	13.48	21.35	
FB-Occ [34]	R101	C	31.50	19.60	20.60	11.30	26.90	29.80	10.40	13.60	13.70	11.40	11.50	20.60	38.20	21.50	24.60	22.70	14.80	21.60	
RenderOcc [35]	R101	C	29.20	19.00	19.70	11.20	28.10	28.20	9.80	14.70	11.80	11.90	13.10	20.10	33.20	21.30	22.60	22.30	15.30	20.90	
GaussianFormer [14]	R101-DCN	C	29.83	19.10	19.52	11.26	26.11	29.78	10.47	13.83	12.58	8.67	12.74	21.57	39.63	23.28	24.46	22.99	9.59	19.12	
Co-Occ [2]	R101	C	30.00	20.30	22.50	11.20	28.60	29.50	9.90	15.80	13.50	8.70	13.60	22.20	34.90	23.10	24.20	24.10	18.00	24.80	
GaussianFormer2-256 [15]	R101-DCN	C	31.74	20.82	21.39	13.44	28.49	30.82	10.92	15.84	13.55	10.53	14.04	22.92	40.61	24.36	26.08	24.27	13.83	21.98	
SurroundOcc [25]	R101-DCN	C	31.49	20.30	20.59	11.68	28.06	30.86	10.70	15.14	14.09	12.06	14.38	22.26	37.29	23.70	24.49	22.77	14.89	21.86	
Inverse++ [13]	R101-DCN	C	31.73	20.91	20.90	13.27	28.40	31.37	11.90	17.76	15.39	13.49	13.32	23.19	39.37	22.85	25.27	23.68	13.43	20.98	
LMSNet [36]	-	L	36.60	14.90	13.10	4.50	14.70	22.10	12.60	4.20	7.20	7.10	12.20	11.50	26.30	14.30	21.10	15.20	18.50	34.20	
L-CONet [31]	-	L	39.40	17.70	19.20	4.00	15.10	26.90	6.20	3.80	6.80	6.00	14.10	13.10	39.70	19.10	24.00	23.90	25.10	35.70	
Co-Occ [2]	-	L	42.20	22.90	22.00	6.90	25.70	32.40	14.50	13.50	21.00	10.50	18.00	22.50	36.60	21.80	24.60	25.70	31.20	39.90	
Co-Occ [2]	R101-DCN	C+L	41.10	27.10	28.10	16.10	34.00	37.20	17.00	21.60	20.80	15.90	21.90	28.70	42.30	25.40	29.10	28.60	28.20	38.00	
GaussianFormer3D [8]	R101-DCN	C+L	43.30	27.10	26.90	15.80	32.70	36.10	18.60	21.70	24.10	13.00	21.30	29.00	40.60	23.70	27.30	28.20	32.60	42.30	
GaussianFormer [1]	R101-DCN	C+R	33.97	20.73	20.46	13.98	27.99	31.52	13.68	18.45	15.79	13.05	13.94	23.84	37.85	19.60	22.41	21.20	16.16	21.81	
OccFusion [1]	R101-DCN	C+L	43.53	27.55	25.15	19.87	34.75	36.21	20.03	23.11	25.25	17.50	22.70	30.06	39.47	23.26	25.68	27.57	29.54	40.60	
OccFusion [1]	R101-DCN	C+L+R	43.96	28.27	28.32	20.95	35.06	36.84	20.33	26.22	25.86	19.17	21.27	30.64	40.08	23.75	25.56	27.63	29.82	40.82	
GaussianFusionOcc [9]	R101-DCN	C+L	45.16	30.21	30.22	18.70	35.91	39.57	22.67	27.36	30.10	18.59	24.45	31.25	43.00	25.76	29.12	29.33	34.65	42.70	
GaussianFusionOcc [9]	R101-DCN	C+L+R	45.20	30.37	30.43	18.54	36.23	39.66	22.57	27.35	30.30	19.14	24.56	31.95	42.60	25.82	29.48	29.70	34.78	42.95	
OccCylindrical [4]	Res-50	C+L	44.94	28.67	26.17	22.12	31.47	36.84	17.95	27.77	29.85	23.90	26.64	38.27	43.00	23.14	27.99	27.81	30.81	40.95	
DAOcc [5]	Res-50	C+L	45.00	30.50	30.80	19.50	34.00	38.80	25.00	27.70	29.90	22.50	23.20	31.60	41.00	25.90	29.40	29.90	35.20	43.50	
TFusionOcc (T-SQ-12800)	Res-50	C+L	46.70	30.76	30.67	21.27	33.12	38.96	22.09	27.54	30.47	22.87	21.65	29.86	42.63	27.18	29.80	30.91	36.81	46.26	
TFusionOcc (T-SQ-IW-12800)	Res-50	C+L	46.92	31.21	31.65	20.13	34.75	39.70	23.08	27.00	30.89	23.33	22.02	30.40	43.11	27.78	30.25	31.47	37.15	46.60	
TFusionOcc (T-P-25600)	Res-50	C+L	45.49	30.04	30.15	19.58	34.20	38.64	22.10	26.60	29.85	22.24	22.44	29.65	41.08	25.19	28.43	29.71	35.77	45.01	
TFusionOcc (T-SQ-25600)	Res-50	C+L	46.14	30.88	30.87	21.26	33.68	39.25	22.54	28.34	31.45	23.61	22.80	30.16	41.76	26.12	29.23	30.26	36.77	46.06	
TFusionOcc (T-SQ-IW-25600)	Res-50	C+L	47.01	31.47	31.96	20.78	34.57	39.73	24.02	27.82	31.19	23.82	23.05	30.67	43.17	27.18	30.13	31.18	37.52	46.71	

TABLE II: 3D semantic occupancy prediction results on SurroundOcc-nuScenes validation set. Our approach outperforms other existing methods with the same input modality. For readers' reference, the bottom of the table presents results from three additional methods using different input modalities. All methods are trained with dense occupancy labels from SurroundOcc [25]. Notion of modality: Camera (C), Lidar (L), Radar (R). The best and second-best performance is indicated in **bold red** and **bold blue**, respectively.

Method	Mask	Backbone	Modality	mIoU	others	barrier	bicycle	bus	car	const. veh.	motorcycle	pedestrian	traffic cone	trailer	truck	drive. surf.	other flat	sidewalk	terrain	manmade	vegetation
MonoScene [27]	✗	Res-101	C	6.06	1.75	7.23	4.26	4.93	9.38	5.67	3.98	3.01	5.90	4.45	7.17	14.91	6.32	7.92	7.43	1.01	7.65
BEVDet [37]	✗	Res-101	C	11.73	2.09	15.29	0.0	4.18	12.97	1.35	0.0	0.43	0.13	6.59	6.66	52.72	19.04	26.45	21.78	14.51	15.26
BEVFormer [29]	✗	Res-101	C	23.67	5.03	38.79	9.98	34.41	41.09	13.24	16.50	18.15	17.83	18.66	27.70	48.95	27.73	29.08	25.38	15.41	14.46
BEVStereo [38]	✗	Res-101	C	24.51	5.73	38.41	7.88	38.70	41.20	17.56	17.33	14.69	10.31	16.84	29.62	54.08	28.92	32.68	26.54	18.74	17.49
TPVFormer [30]	✗	Res-101	C	28.34	6.67	39.20	14.24	41.54	46.98	19.21	22.64	17.87	14.54	30.20	35.51	56.18	33.65	35.69	31.61	19.97	16.12
OccFormer [33]	✗	Res-101	C	21.93	5.94	30.29	12.32	34.40	39.17	14.44	16.45	17.22	9.27	13.90	26.36	50.99	30.96	34.66	22.73	6.76	6.97
RenderOcc [35]	✗	Res-101	C	26.11	4.84	31.72	10.72	27.67	26.45	13.87	18.20	17.67	17.84	21.19	23.25	63.20	36.42	46.21	44.26	19.58	20.72
CTF-Occ [26]	✗	Res-101	C	28.53	8.09	39.33	20.56	38.29	42.24	16.93	24.52	22.72	21.05	22.98	31.11	53.33	33.84	37.98	33.23	20.79	18.00
Inverse++ [13]	✗	Res-101	C	31.04	9.56	41.91	23.53	42.38	46.35	18.61	28.03	26.61	24.77	25.93	34.81	60.10	33.23	37.62	34.83	19.20	20.26
RadOcc [39]	✓	Swin-B	C+L	49.38	10.90	58.20	25.00	57.90	62.90	34.00	33.50	50.10	32.10	48.90	52.10	82.90	42.70	55.30	58.30	68.60	66.00
OccFusion [1]	✓	R101-DCN	C+L+R	46.67	12.40	50.30	31.50	57.60	58.80	34.00	41.00	47.20	29.70	42.00	48.00	78.40	35.70	47.30	52.70	63.50	63.30
OccFusion [1]	✓	R101-DCN	C+L	48.74	12.40	51.80	33.00	54.60	57.70	34.00	43.00	48.40	35.50	41.20	48.60	83.00	44.70	57.10	60.00	62.50	61.30
GaussianFormer3D [8]	✓	R101-DCN	C+L	46.40	9.80	50.00	31.30	54.00	59.40	28.10	36.20	46.20	26.70	40.20	49.70	79.10	37.30	49.00	55.00	69.10	67.60
RM ² Occ [40]	✓	R101-DCN	C+L	47.82	13.34	54.53	33.81	58.30	59.97	34.45	34.89	29.43	31.53	39.91	42.44	96.01	49.76	61.28	53.71	51.96	51.96
SDGOcc [6]	✓	Res-50	C+L	51.66	13.20	57.80	24.30	60.30	64.30	36.20	39.40	52.40	35.80	50.90	53.70	84.60	47.50	58.00	61.60	70.70	67.70
EFPOcc [7]	✓	Res-50	C+L	52.82	12.09	59.67	33.39	61.76	64.98	35.46	46.01	57.09	41.04	47.87	54.59	82.76	43.95	56.37	60.23	71.12	69.60
TFusionOcc																					

Method	Backbone	Modality	IoU	mIoU	barrier	bicycle	bus	car	const. veh.	motorcycle	pedestrian	traffic cone	trailer	truck	drive. surf.	other flat	sidewalk	terrain	manmade	vegetation
InverseMatrixVT3D [32]	R101-DCN	C	29.72 (-0.31%)	18.99 (+0.11%)	18.55	14.29	22.28	30.02	10.19	15.20	10.03	9.71	13.28	20.98	37.18	23.47	27.74	17.46	10.36	23.13
GaussianFormer [14]	R101-DCN	C	27.37 (-2.46%)	16.96 (-2.14%)	18.16	9.58	21.09	26.83	8.04	10.13	7.80	5.84	12.66	18.24	35.53	18.51	27.79	19.23	11.04	20.85
Co-Occ [2]	R101	C	28.90 (-1.10%)	19.70 (-0.60%)	22.10	17.60	26.30	30.80	10.90	9.90	8.20	9.70	11.40	19.30	39.00	22.20	32.60	23.00	11.50	21.30
GaussianFormer2-256 [15]	R101-DCN	C	31.14 (-0.60%)	20.36 (-0.46%)	19.84	13.52	26.89	31.65	10.82	15.16	9.04	8.41	13.72	21.84	40.51	24.57	32.21	20.65	12.64	24.33
SurroundOcc [25]	R101-DCN	C	30.57 (-0.92%)	19.85 (-0.45%)	21.40	12.75	25.49	31.31	11.30	12.65	8.94	9.48	14.51	21.52	35.34	25.32	29.89	18.37	14.44	24.78
Inverse++ [13]	R101-DCN	C	31.32 (-0.41%)	20.66 (-0.25%)	22.52	13.79	25.49	31.80	11.70	16.72	11.14	10.12	12.29	22.25	38.78	23.93	31.62	21.14	12.65	24.61
Co-Occ [2]	R101	C+L	40.30 (-0.80%)	26.60 (-0.50%)	26.60	19.10	37.60	37.20	15.90	20.30	16.30	12.30	23.30	37.00	41.00	22.80	35.20	24.60	27.80	39.30
OccFusion [1]	R101-DCN	C+L	42.67 (-0.86%)	26.68 (-0.87%)	20.91	18.39	35.26	36.19	17.69	19.05	17.08	23.86	38.28	26.37	31.44	21.35	29.48	43.22		
OccFusion [1]	R101-DCN	C+L+R	42.67 (-1.29%)	27.39 (-0.88%)	27.82	21.10	36.00	37.10	17.23	21.67	20.34	17.46	20.93	38.57	38.99	24.72	31.96	21.26	29.64	43.53
GaussianFusionOcc [9]	R101-DCN	C+L+R	44.28 (-0.88%)	29.19 (-1.02%)	28.10	19.84	36.28	38.90	18.11	21.13	26.14	17.95	25.79	29.92	41.72	27.35	34.99	22.85	33.84	44.10
GaussianFusionOcc [9]	R101-DCN	C+L+R	44.36 (-0.84%)	29.86 (-0.51%)	28.40	19.88	38.87	39.33	20.61	26.05	25.66	17.97	26.07	31.02	41.70	24.94	35.27	24.08	33.90	44.00
OccCylindrical [4]	Res-50	C+L	44.08 (-0.86%)	28.07 (-0.60%)	24.50	22.66	33.47	36.79	16.96	23.63	23.79	23.49	22.70	28.14	41.67	22.32	33.55	21.44	30.58	43.45
DAOcc [5]	Res-50	C+L	44.51 (-0.49%)	29.65 (-0.85%)	28.50	19.63	38.01	38.98	21.42	20.19	24.63	21.52	23.60	31.12	40.56	26.68	35.05	24.94	34.29	45.28
TFusionOcc (T-SQ-12800)	Res-50	C+L	45.79 (-0.91%)	30.28 (-0.48%)	29.32	22.08	35.67	38.47	18.43	23.29	26.19	24.65	23.34	28.40	41.79	28.40	34.99	26.16	35.75	47.54
TFusionOcc (T-SQ-IW-12800)	Res-50	C+L	45.81 (-1.11%)	30.74 (-0.47%)	30.54	21.85	37.99	39.11	20.43	21.56	26.44	24.82	23.39	28.74	41.99	28.68	35.70	26.86	36.08	47.63
TFusionOcc (T-P-25600)	Res-50	C+L	44.77 (-0.72%)	29.22 (-0.82%)	27.86	21.11	36.24	38.33	17.79	18.33	25.25	23.53	25.50	28.59	40.27	24.95	33.54	24.82	34.90	46.57
TFusionOcc (T-SQ-25600)	Res-50	C+L	45.40 (-0.74%)	30.38 (-0.50%)	29.18	22.52	36.87	38.61	19.41	22.19	26.98	24.84	24.78	28.70	41.21	27.39	34.74	25.57	35.69	47.44
TFusionOcc (T-SQ-IW-25600)	Res-50	C+L	46.25 (-0.76%)	30.82 (-0.65%)	30.38	21.70	38.23	39.28	20.29	19.78	26.75	25.35	24.88	29.05	42.35	28.14	35.91	26.52	36.49	48.01

TABLE IV: 3D semantic occupancy prediction results on SurroundOcc-nuScenes validation rainy scenario subset. All methods are trained with dense occupancy labels from SurroundOcc [25]. Notion of modality: Camera (C), Lidar (L), Radar (R). The best and second-best performance is indicated in **bold red** and **bold blue**, respectively.

Method	Backbone	Modality	IoU	mIoU	barrier	bicycle	bus	car	const. veh.	motorcycle	pedestrian	traffic cone	trailer	truck	drive. surf.	other flat	sidewalk	terrain	manmade	vegetation
InverseMatrixVT3D [32]	R101-DCN	C	22.48 (-7.55%)	9.99 (-8.89%)	10.40	12.03	0.00	29.94	0.00	9.92	4.88	0.91	0.00	17.79	29.10	2.37	10.80	9.40	8.68	13.57
GaussianFormer [14]	R101-DCN	C	20.30 (-9.53%)	9.07 (-10.03%)	6.11	8.70	0.00	25.75	0.00	10.44	2.85	0.55	0.00	17.26	30.95	2.95	12.53	9.94	6.65	10.71
Co-Occ [2]	R101	C	18.90 (-11.10%)	9.40 (-10.90%)	4.50	9.30	0.00	29.50	0.00	8.40	3.50	0.00	0.00	15.10	29.40	0.60	12.40	11.50	10.70	15.50
GaussianFormer2-256 [15]	R101-DCN	C	21.19 (-10.55%)	10.14 (-10.68%)	5.25	9.29	0.00	29.33	0.00	13.65	5.80	0.90	0.00	20.22	31.80	1.94	14.83	10.48	5.96	12.72
SurroundOcc [25]	R101-DCN	C	24.38 (-7.11%)	10.80 (-9.50%)	10.55	14.60	0.00	31.05	0.00	8.26	5.37	0.58	0.00	18.75	30.72	2.74	12.39	11.53	10.52	15.77
Inverse++ [13]	R101-DCN	C	23.70 (-8.03%)	10.93 (-9.98%)	8.87	10.19	0.00	32.62	0.00	11.77	7.46	0.72	0.00	22.20	32.95	2.15	13.01	9.79	8.61	14.48
Co-Occ [2]	R101	C+L	35.60 (-5.50%)	14.60 (-12.50%)	8.40	16.40	0.00	37.20	0.00	13.80	10.90	0.40	0.00	24.30	36.40	2.20	14.60	17.00	19.90	31.70
OccFusion [1]	R101-DCN	C+L	40.87 (-2.66%)	15.87 (-11.68%)	13.28	17.53	0.00	36.42	0.00	16.16	11.37	1.42	0.00	25.71	32.64	0.63	16.06	20.87	24.52	37.27
OccFusion [1]	R101-DCN	C+L+R	41.01 (-2.95%)	16.61 (-11.68%)	15.70	16.26	0.00	38.09	0.00	22.18	13.24	0.08	0.00	25.92	33.15	1.57	16.08	21.09	24.51	37.83
GaussianFusionOcc [9]	R101-DCN	C+L+R	42.78 (-2.38%)	18.66 (-11.55%)	16.09	12.27	0.00	39.82	0.00	27.66	13.68	0.07	0.00	38.25	40.10	2.07	19.64	19.82	29.55	39.61
GaussianFusionOcc [9]	R101-DCN	C+L+R	42.51 (-2.69%)	18.45 (-11.92%)	12.15	11.47	0.00	39.77	0.00	29.58	15.27	0.04	0.00	37.08	37.13	2.58	19.94	20.63	29.42	40.10
OccCylindrical [4]	Res-50	C+L	43.38 (-1.56%)	17.79 (-10.88%)	16.19	10.04	0.00	37.84	0.00	25.63	13.28	0.23	0.00	32.93	39.59	3.89	17.89	21.61	26.99	38.47
DAOcc [5]	Res-50	C+L	42.85 (-2.15%)	18.53 (-11.97%)	17.18	15.07	0.00	39.05	0.00	25.77	14.70	0.07	0.00	32.51	33.95	4.02	19.78	22.58	30.91	40.87
TFusionOcc (T-SQ-12800)	Res-50	C+L	44.74 (-1.96%)	18.81 (-11.95%)	16.01	17.51	0.00	39.84	0.00	23.82	12.76	1.13	0.00	32.79	37.67	3.48	19.70	21.42	31.41	43.40
TFusionOcc (T-SQ-IW-12800)	Res-50	C+L	44.82 (-2.10%)	19.07 (-12.14%)	16.81	15.53	0.00	40.36	0.00	21.27	13.33	3.79	0.00	34.89	38.04	3.92	19.86	21.89	31.67	43.72
TFusionOcc (T-P-25600)	Res-50	C+L	43.25 (-2.24%)	17.83 (-12.21%)	14.12	10.10	0.00	38.45	0.00	21.99	13.10	1.16	0.00	32.05	34.60	4.61	18.91	23.14	30.76	42.35
TFusionOcc (T-SQ-25600)	Res-50	C+L	43.86 (-2.28%)	18.95 (-11.93%)	17.10	16.09	0.00	40.17	0.00	23.21	15.13	2.97	0.00	33.83	36.18	3.75	20.12	20.48	31.30	42.94
TFusionOcc (T-SQ-IW-25600)	Res-50	C+L	44.97 (-2.04%)	19.67 (-11.80%)	17.98	19.96	0.00	40.69	0.00	23.30	14.76	3.85	0.00	34.49	38.35	3.43	19.70	22.42	31.95	43.79

TABLE V: 3D semantic occupancy prediction results on SurroundOcc-nuScenes validation night scenario subset. All methods are trained with dense occupancy labels from SurroundOcc [25]. Notion of modality: Camera (C), Lidar (L), Radar (R). The best and second-best performance is indicated in **bold red** and **bold blue**, respectively.

Method	Metric	Clean	Cam Crash	Frame Lost	Color Quant	Motion Blur	Bright	Low Light	Fog	Snow
SurroundOcc	mIoU	20.30	11.60 (-8.70%)	10.00 (-10.30%)	14.03 (-6.27%)	12.41 (-7.89%)	19.18 (-1.12%)	12.15 (-8.15%)	18.42 (-1.88%)	7.39 (-12.91%)
Inverse++	mIoU	20.91	11.76 (-9.15%)	10.22 (-10.69%)	14.88 (-6.03%)	12.84 (-8.07%)	19.71 (-1.20%)	12.05 (-8.86%)	18.86 (-2.05%)	7.62 (-13.29%)
OccCylindrical	mIoU	28.67	23.38 (-5.29%)	21.87 (-6.80%)	25.38 (-3.29%)	22.57 (-6.10%)	27.88 (-0.79%)	22.17 (-6.50%)	27.38 (-1.29%)	18.29 (-10.38%)
DAOcc	mIoU	30.50	22.35 (-8.15%)	20.78 (-9.72%)	27.46 (-3.04%)	26.25 (-4.25%)	26.78 (-3.72%)	21.15 (-9.35%)	26.87 (-3.63%)	19.42 (-11.08%)
TFusionOcc (T-P-25600)	mIoU	30.04	22.34 (-7.70%)	20.78 (-9.26%)	24.42 (-5.62%)	20.04 (-10.00%)	29.03 (-1.01%)	18.62 (-11.42%)	27.43 (-2.61%)	15.62 (-14.42%)
TFusionOcc (T-SQ-25600)	mIoU	30.88	23.50 (-7.38%)	22.04 (-8.84%)	25.65 (-5.23%)	20.25 (-10.63%)	29.92 (-0.96%)	20.98 (-9.90%)	28.85 (-2.03%)	16.33 (-14.55%)
TFusionOcc (T-SQ-IW-25600)	mIoU	31.47	24.39 (-7.08%)	23.03 (-8.44%)	26.14 (-5.33%)	21.06 (-10				

Method	Metric	Clean	Beam Missing	Cross Sensor	Cross Talk	Incomplete Echo	Motion Blur	Wet Ground	Fog	Snow
OccCylindrical	mIoU	24.06	19.83 (-4.23%)	16.20 (-7.86%)	22.60 (-1.46%)	20.93 (-3.13%)	20.85 (-3.21%)	23.31 (-0.75%)	17.32 (-6.74%)	22.38 (-1.68%)
DAcc	mIoU	27.73	22.96 (-4.77%)	18.41 (-9.32%)	22.86 (-4.87%)	24.45 (-3.28%)	23.66 (-4.07%)	27.25 (-0.48%)	19.73 (-8.00%)	24.53 (-3.20%)
TFusionOcc (T-P-25600)	mIoU	26.13	20.49 (-5.64%)	15.38 (-10.75%)	23.76 (-2.37%)	22.69 (-3.44%)	21.39 (-4.74%)	25.05 (-1.08%)	17.44 (-8.69%)	23.15 (-2.98%)
TFusionOcc (T-SQ-25600)	mIoU	27.03	21.07 (-5.96%)	15.61 (-11.42%)	24.73 (-2.30%)	23.30 (-3.73%)	22.15 (-4.88%)	26.06 (-0.97%)	18.40 (-8.63%)	24.37 (-2.66%)
TFusionOcc (T-SQ-IW-25600)	mIoU	27.50	21.81 (-5.69%)	16.49 (-11.01%)	24.94 (-2.56%)	24.11 (-3.39%)	22.62 (-4.88%)	26.57 (-0.93%)	18.63 (-8.87%)	24.37 (-3.13%)

TABLE IX: 3D semantic occupancy prediction mIoU results on nuScenes-C Lidar Corruption benchmark. All methods are evaluated with different corruption type input lidar point cloud provided by nuScenes-C [11] and ground-truth occupancy labels from SurroundOcc [25].

Corruption	Severity	IoU	mIoU	barrier	bicycle	bus	car	const. veh.	motorcycle	pedestrian	traffic cone	trailer	truck	drive. surf.	other flat	sidewalk	terrain	mannade	vegetation
				●	●	●	●	●	●	●	●	●	●	●	●	●	●	●	●
CameraCrash	Easy	43.16	26.44	23.34	16.62	28.80	35.79	19.34	21.30	28.47	19.01	18.46	24.14	36.89	19.19	25.07	27.42	35.32	43.94
CameraCrash	Mid	42.27	23.37	17.66	11.56	26.79	33.91	14.58	16.88	26.48	16.44	13.69	19.75	35.87	16.54	22.43	24.70	34.07	42.56
CameraCrash	Hard	42.39	23.35	20.30	11.23	26.54	34.40	15.27	13.93	25.80	17.87	11.15	21.39	35.24	14.59	22.44	25.18	34.52	43.77
FrameLost	Easy	44.33	27.42	25.40	16.12	30.44	36.89	19.15	21.10	28.59	20.72	18.97	26.33	38.65	21.48	26.20	28.11	35.81	44.84
FrameLost	Mid	41.33	22.19	15.55	10.88	24.67	33.26	13.95	14.55	25.62	15.66	11.70	19.94	33.63	13.21	21.59	24.17	33.98	42.73
FrameLost	Hard	39.66	19.48	9.91	9.09	22.02	31.26	11.74	11.63	23.98	12.70	8.77	15.30	30.99	9.11	18.80	21.75	33.03	41.52
ColorQuant	Easy	46.55	30.61	31.18	19.09	33.46	39.63	22.86	26.15	30.57	23.20	22.87	30.29	42.26	25.40	28.71	30.42	37.19	46.44
ColorQuant	Mid	44.19	26.96	25.94	14.03	30.21	38.26	19.43	18.13	29.03	22.00	18.56	26.63	38.54	19.68	24.39	26.26	35.72	44.54
ColorQuant	Hard	41.18	20.85	13.87	8.24	22.61	34.82	12.93	8.22	26.70	18.66	9.86	20.29	33.70	9.37	19.14	33.79	42.30	20.85
MotionBlur	Easy	41.43	26.89	28.45	15.39	31.42	37.33	20.59	19.98	29.74	23.25	19.18	25.99	36.16	17.03	22.63	25.86	34.73	42.48
MotionBlur	Mid	37.26	18.80	15.08	8.51	21.43	33.12	11.83	13.43	22.58	17.93	6.36	13.80	29.91	3.61	12.99	20.31	31.56	38.34
MotionBlur	Hard	37.06	17.48	12.18	7.54	19.65	32.08	9.80	12.42	20.60	16.37	4.50	12.63	29.47	2.63	11.26	19.46	31.17	37.93
Brightness	Easy	46.90	31.35	31.83	20.44	34.29	39.73	23.55	27.70	31.19	23.89	23.07	30.52	43.06	27.37	29.94	30.92	37.45	46.57
Brightness	Mid	46.45	30.67	31.12	19.86	32.69	39.37	22.29	26.38	31.08	23.73	22.70	29.40	42.35	27.07	28.96	30.20	37.26	46.31
Brightness	Hard	45.59	29.71	30.29	19.08	31.22	38.80	20.78	25.06	30.92	23.76	21.97	28.14	40.90	25.49	27.29	28.93	36.92	45.88
LowLight	Easy	43.86	25.38	19.52	14.11	30.88	37.84	20.19	25.19	28.43	17.38	13.94	25.64	37.39	15.11	23.22	25.82	35.57	44.48
LowLight	Mid	42.12	21.69	11.25	11.54	27.65	36.35	11.88	18.08	26.75	12.07	5.65	22.09	34.43	8.43	19.90	23.02	34.45	43.44
LowLight	Hard	40.60	17.93	3.52	6.49	23.37	34.05	7.87	15.49	23.81	5.33	1.57	17.02	32.01	3.56	16.69	20.34	33.18	42.59
Fog	Easy	46.37	30.57	30.82	19.55	34.30	39.40	21.91	25.99	30.65	23.35	22.12	30.06	42.13	26.77	28.91	29.86	37.10	46.27
Fog	Mid	46.03	29.89	30.01	18.93	33.72	39.29	20.89	25.12	30.42	22.91	21.21	29.32	41.37	25.36	27.89	28.93	36.87	46.07
Fog	Hard	45.44	28.61	29.00	17.43	32.02	38.90	18.92	24.15	30.04	22.41	19.61	27.90	40.02	22.29	25.69	27.37	36.47	45.58
Snow	Easy	41.26	20.46	12.34	8.18	24.01	34.48	14.53	13.38	26.04	20.12	6.13	19.37	32.52	6.58	12.73	21.68	33.02	42.31
Snow	Mid	39.61	15.81	7.13	4.17	16.34	30.79	7.63	11.86	22.00	16.87	4.93	9.97	27.63	2.30	7.69	15.13	30.04	38.46
Snow	Hard	40.23	16.08	5.29	4.19	16.00	31.17	8.68	11.28	22.39	16.59	4.58	10.08	29.80	2.64	9.17	14.27	31.40	39.78

TABLE X: The performance of TFusionOcc(T-SQ-IW-25600) on the nuScene-C [11] dataset under different camera corruption and severity settings.

Corruption	Severity	IoU	mIoU	barrier	bicycle	bus	car	const. veh.	motorcycle	pedestrian	traffic cone	trailer	truck	drive. surf.	other flat	sidewalk	terrain	mannade	vegetation
				●	●	●	●	●	●	●	●	●	●	●	●	●	●	●	●
BeamMissing	Light	38.03	24.83	25.39	12.35	30.38	33.20	17.80	20.84	23.97	16.98	19.35	26.19	37.83	21.87	23.66	24.77	26.92	35.79
BeamMissing	Moderate	34.28	21.94	22.45	9.84	28.26	29.26	15.39	17.79	20.83	12.97	17.61	23.96	35.44	19.69	20.99	22.06	23.07	31.41
BeamMissing	Heavy	29.97	18.67	18.85	6.93	25.51	24.95	13.02	13.23	15.80	11.40	15.58	21.18	32.63	17.35	18.16	18.45	19.03	26.71
CrossSensor	Light	31.71	20.08	19.55	7.95	27.85	27.18	14.63	13.75	17.86	11.99	17.34	23.06	34.50	19.05	19.57	19.78	20.08	27.19
CrossSensor	Moderate	26.52	16.07	15.50	5.00	23.42	21.71	12.15	7.42	13.75	9.30	14.33	19.55	31.52	15.85	16.60	16.43	14.97	19.66
CrossSensor	Heavy	22.23	13.32	11.50	3.77	21.31	16.56	6.96	9.04	10.43	7.01	13.48	15.76	28.99	14.64	14.00	13.66	11.28	14.64
CrossTalk	Light	39.77	26.33	28.50	14.08	31.14	35.44	18.51	21.00	25.73	17.29	19.97	27.30	39.52	24.07	26.08	27.46	29.48	35.63
CrossTalk	Moderate	37.47	24.93	27.82	12.62	30.10	34.11	16.63	19.01	24.07	15.91	19.14	26.14	38.85	23.78	25.07	26.82	28.03	30.82
CrossTalk	Heavy	35.26	23.57	26.75	11.55	29.19	32.80	15.39	16.61	22.60	14.60	18.47	25.09	38.09	23.34	23.41	25.86	26.44	26.93
IncompleteEcho	Light	41.18	25.74	28.97	12.08	28.39	30.45	15.70	19.21	27.68	19.35	17.63	24.15	39.80	23.88	26.37	27.75	30.51	39.94
IncompleteEcho	Moderate	41.01	24.66	28.96	10.54	25.72	26.81	13.15	17.27	27.67	19.26	15.40	21.58	39.74	23.90	26.36	27.73	30.52	39.93
IncompleteEcho	Heavy	40.62	21.93	28.92	8.66	17.25	16.89	7.41	13.52	27.62	19.08	8.97	14.64	39.57	23.92	26.34	27.71	30.53	39.91
MotionBlur	Light	38.10	24.89	25.61	12.99	30.89	33.74	19.39	20.91	24.15	14.99	19.40	26.77	36.30	21.25	23.10	24.59	26.09	38.00
MotionBlur	Moderate	35.44	22.56	22.40	11.01	29.50	31.09	18.24	18.10	20.87	11.53	18.13	25.43	33.88	18.98	20.68	22.26	22.74	36.10
MotionBlur	Heavy	33.07	20.42	19.24	9.15	28.01	28.37	17.26	15.57	17.81	8.80	16.49	23.64	32.07	17.44	18.77	20.20	19.85	34.03
WetGround	Light	40.53	26.99	28.86	15.18	31.66	36.33	19.80	23.18	27.60	19.65	20.73	28.03	37.07	21.62	23.82	27.84	30.50	39.99
WetGround	Moderate	39.84	26.57	28.86	15.12	31.65	36.23	19.77	22.70	27.53	19.86	20.71	27.91	35.13	19.21	21.98	28.01	30.50	39.98
WetGround	Heavy	39.14	26.14	28.80	14.79	31.57	36.14	19.74	22.69	27.47	19.87	20.68	27.85	33.08	17.10	20.01			

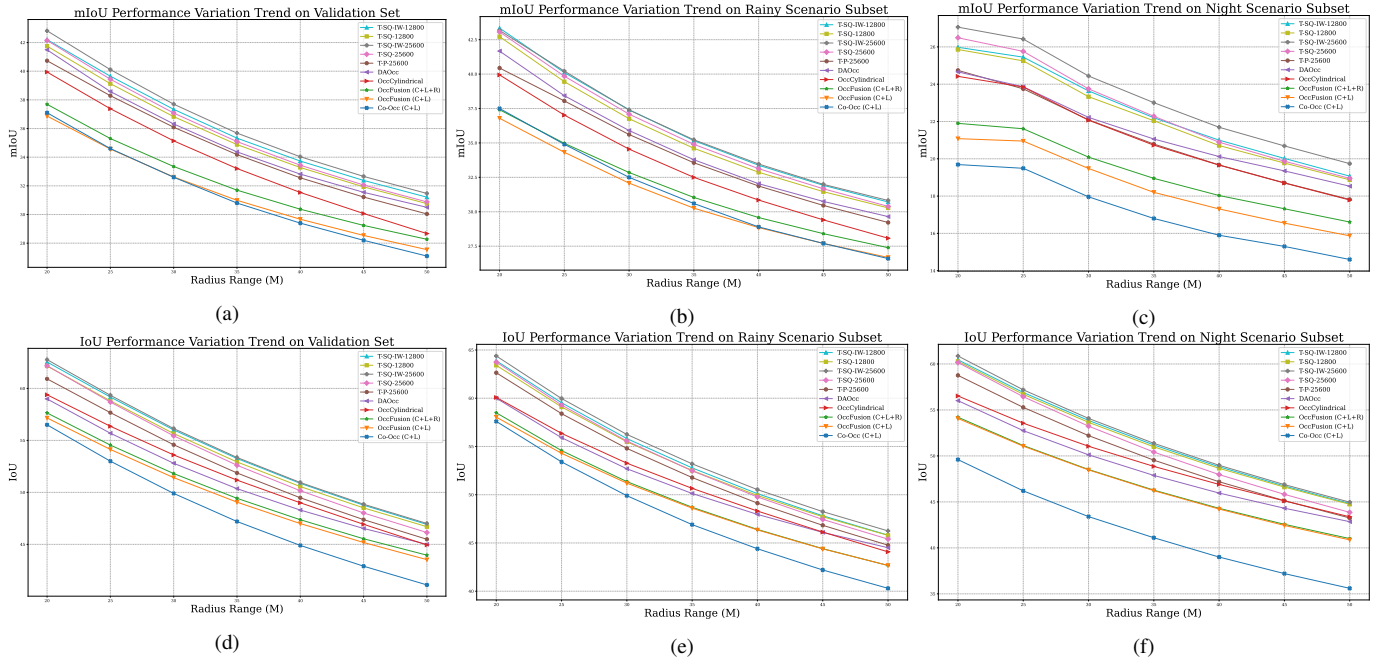


Fig. 10: Performance variation trend for 3D semantic occupancy prediction task. (a) mIoU performance variation trend on the whole SurroundOcc-nuScenes validation set, (b) IoU performance variation on the whole SurroundOcc-nuScenes validation set, (c) mIoU performance variation trend on the SurroundOcc-nuScenes validation rainy scenario subset, (d) IoU performance variation on the SurroundOcc-nuScenes validation rainy scenario subset, (e) mIoU performance variation on the SurroundOcc-nuScenes validation night scenario subset, and (f) IoU performance variation on the SurroundOcc-nuScenes validation night scenario subset. **Better viewed when zoomed in.**

settings achieved par performance with DAOcc and OccCylindrical, as shown in Figure 11c. Regarding the geometry prediction capability measured under the IoU criterion, our approach in all settings outperforms the others in the sector ranges 0~10m, 10~20m and 20~30m. Nevertheless, our approach lags behind other SOTA algorithms when the perception sector range reaches 30~40m and 40~50m as shown in Figure 11f.

I. Qualitative Study

1) *Qualitative Results On SurroundOcc-nuScenes Dataset:* To qualitatively study the difference in each setting of the proposed TFusionOcc, we demonstrate the visualization result of each setting in daytime, rainy, and night-time scenarios in Figure 12, with the main discrepancy area highlighted. In the daytime scenarios as shown at the top of Figure 12, in the orange square highlighted area, except for the T-P-25600 setting, all other settings successfully detect those two pedestrians. What is more, T-SQ-IW Primitive preserves better the geometric contour shape of background buildings, such as sharper building edges and more accurate building boundaries, than T-P primitive and T-SQ primitive, demonstrating the importance of the geometric shape flexibility of intermediate primitives. In rainy scenarios, as shown in the middle of Figure 12, in the dark red square highlighted area. The better geometric shape representation capability of the primitives could more accurately capture the geometric structure of the object, leading to better detection performance; T-SQ-IW-25600 achieved the best performance due to its best geometric shape representation capability, and T-P-25600 the worst,

stemming from the ellipsoid geometric shape prior. Similarly, in the nighttime scenarios, as shown in the bottom of Figure 12, in the square highlighted area. Even with severe occlusions and a vehicle headlight glare pollution problem, we observed that greater geometric shape flexibility of primitives leads to better detection performance, which aligns with rainy and daytime phenomena.

Furthermore, to demonstrate the effectiveness and robustness of our method, we compare TFusionOcc in three different T-Primitive settings, such as T-P-25600, T-SQ-25600 and T-SQ-IW-25600, against other SOTA algorithms in challenging daytime, rainy and nighttime scenarios, as shown in Figure 13, with the primary difference area highlighted in each scenario. In the daytime scenario, as shown at the top of Figure 13, in the orange square highlighted area, benefit from multi-task learning, which provides an additional supervision signal, DAOcc successfully detects distant pedestrians and achieves similar performance as TFusionOcc. However, in the dark-red-square-highlighted area, DAOcc fails to detect the distant vehicle, demonstrating the superior performance of our proposed method. In the rainy scenario, as shown in the middle of Figure 13, in the purple square highlighted area, our proposed method not only successfully detects all dynamic objects, but also preserves their general contours well. In the highlighted dark-blue-square area, our approach achieves par performance with other SOTA algorithms for detecting challenging pedestrians. In the nighttime scenario, as shown at the bottom of Figure 13, our proposed method successfully detects very distant dynamic objects in the highlighted dark-red-square area, demonstrating its superior long-range dynamic object perception capability.

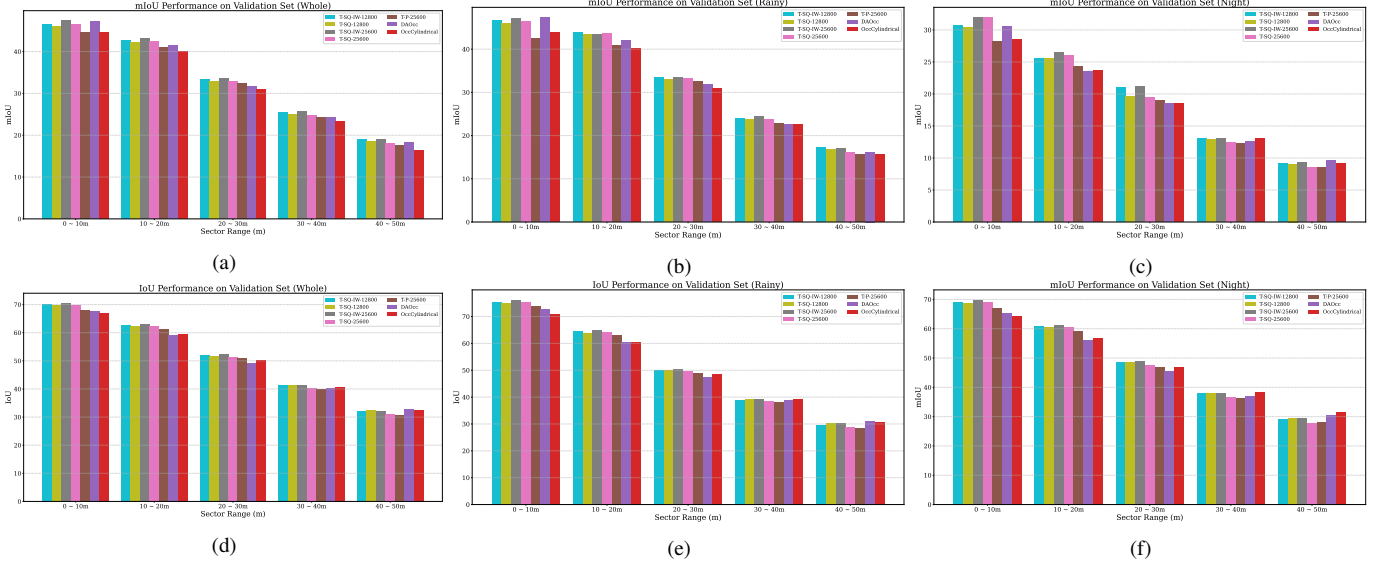


Fig. 11: Performance at different sector ranges for the 3D semantic occupancy prediction task. (a) mIoU performance at different sector ranges on the whole SurroundOcc-nuScenes validation set, (b) IoU performance at different sector ranges on the whole SurroundOcc-nuScenes validation set, (c) mIoU performance at different sector ranges on the SurroundOcc-nuScenes validation rainy scenario subset, (d) IoU performance at different sector ranges on the SurroundOcc-nuScenes validation rainy scenario subset, (e) mIoU performance at different sector ranges on the SurroundOcc-nuScenes validation night scenario subset, and (f) IoU performance at different sector ranges on the SurroundOcc-nuScenes validation night scenario subset. **Better viewed when zoomed in.**

2) *Qualitative Results On nuScenes-C Dataset:* Since the nuScenes dataset does not contain fog and snow scenarios, which are common driving conditions in the real world, we adopted the nuScenes-C dataset to evaluate our model across three settings within the same scene under fog and snow conditions, with the severity of each condition set to hard, and compare the visualization results with other SOTA algorithms. The visualization results are shown in Figure 14, with the main area of the discrepancy highlighted in dark blue and dark red squares.

Under foggy conditions, the surround-view images suffer significant visibility degradation due to strong atmospheric scattering, leading to reduced illumination, low contrast, and severely blurred object boundaries, especially in distant regions of the scene. Compared to baseline SOTA algorithms, our method, especially the T-SQ-IW-25600 setting, successfully detects all dynamic pedestrian objects in the scene (as shown by the dark blue squares) and also accurately captures the background objects' contour as well (as shown by the dark red squares), demonstrating the robustness of the proposed algorithm under foggy conditions. Nevertheless, in the snow condition, the snowfall captured in the surround-view image appears to introduce salt-and-pepper noise to the image, and snowflakes occlude some objects' contours, even the main body parts. In this case, our proposed method is less tolerant of salt-and-pepper noise than the baseline SOTA algorithms.

J. Model Efficiency

We evaluated the real-time performance of our model in various settings on an RTX 4090 GPU and presented the results in Table XII. The experiment results show the trade-off between the total number of primitives and the model inference speed.

Method	Modality	Latency (ms) (↓)	Memory (GB) (↓)	Params
SurroundOcc* [25]	C	472	5.98	180.51M
InverseMatrixVT3D* [32]	C	447	4.41	67.18M
OccFusion(C+R)* [1]	C+R	588	5.56	92.71M
OccFusion(C+L)* [1]	C+L	591	5.56	92.71M
OccFusion(C+L+R)* [1]	C+L+R	601	5.78	114.97M
OccCylindrical* [4]	C+L	398	10.63	111.62M
TFusionOcc (T-SQ-12800)	C+L	278.46	3.68	95.62M
TFusionOcc (T-SQ-IW-12800)	C+L	281.47	3.88	95.96M
TFusionOcc (T-P-25600)	C+L	385.49	4.73	97.51M
TFusionOcc (T-SQ-25600)	C+L	388.05	4.13	97.59M
TFusionOcc (T-SQ-IW-25600)	C+L	391.06	4.04	98.24M

TABLE XII: Efficiency comparison of multi-modal 3D semantic occupancy prediction on the nuScenes validation set. Algorithm results marked with * were taken from the paper that introduced the model and were measured on a different GPU.

More primitives require more rendering operations, leading to higher latency. Surprisingly, all five settings have similar total model parameters. Based on the main performance benchmark shown in Table II, the T-SQ-IW-12800 setting delivers the best balance between detection and real-time performance.

K. Ablation Study

Main-Skele	Augment	Overlap Remove	Range Filter	IoU (↑)	mIoU (↑)
✓	✓	✓	✓	46.24 (Baseline)	30.79 (Baseline)
✓	✓	✗	✓	46.20 (-0.04%)	30.70 (-0.09%)
✓	✓	✓	✗	46.07 (-0.17%)	30.76 (-0.03%)
✓	✓	✗	✗	46.08 (-0.16%)	30.69 (-0.1%)
✓	✗	✗	✗	41.96 (-4.28%)	29.92 (-0.87%)
✗	✓	✗	✗	29.35 (-16.89%)	22.31 (-8.48%)

TABLE XIII: Ablation study on the Skeleton Merge Module. Main-Skele: Lidar-side main skeleton branch. Augment: Camera-side augment skeleton branch. ↑:the higher, the better.

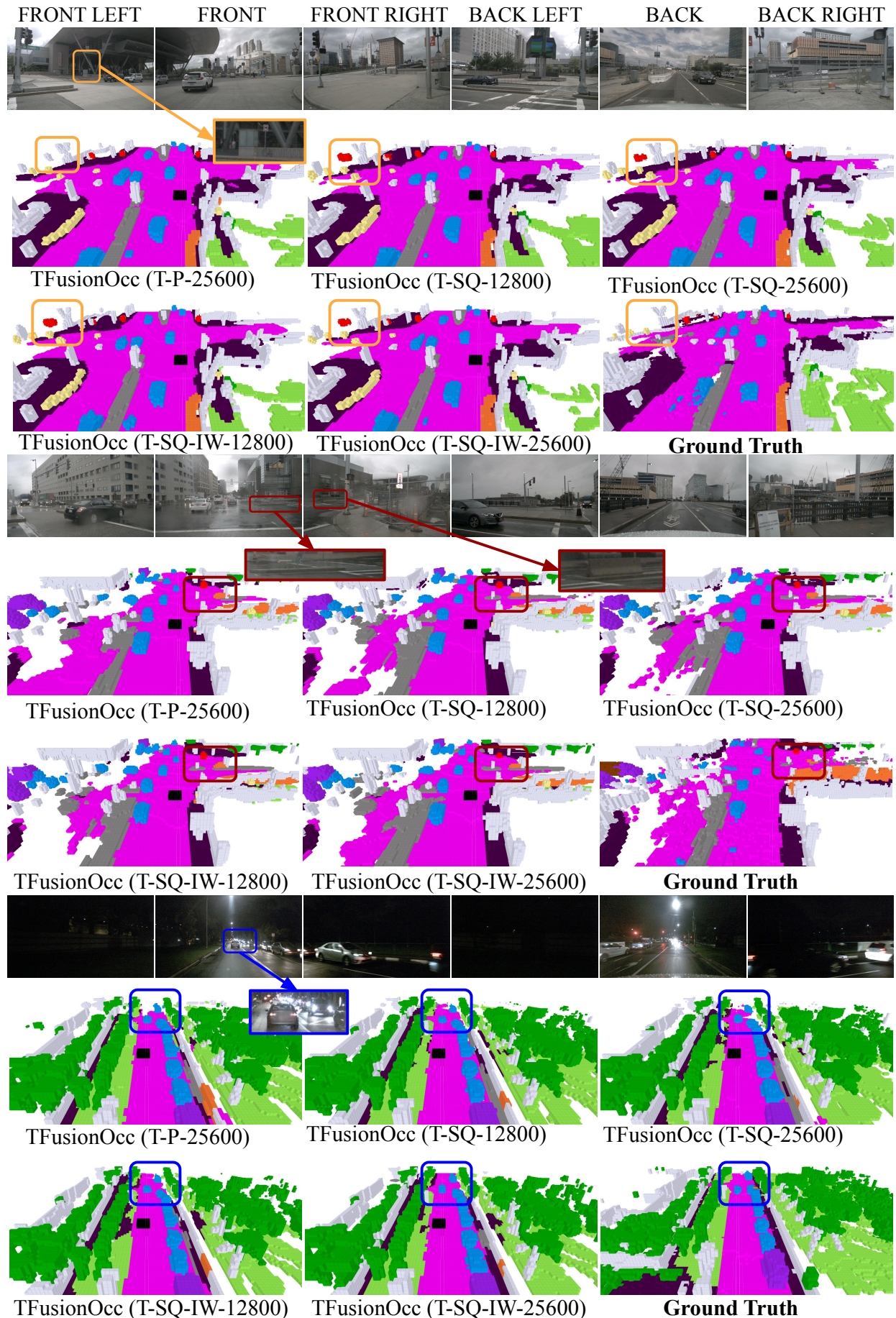


Fig. 12: Qualitative results under different settings for daytime, rainy, and nighttime scenarios displayed in the upper, middle, and bottom sections, respectively. **Better viewed when zoomed in.**

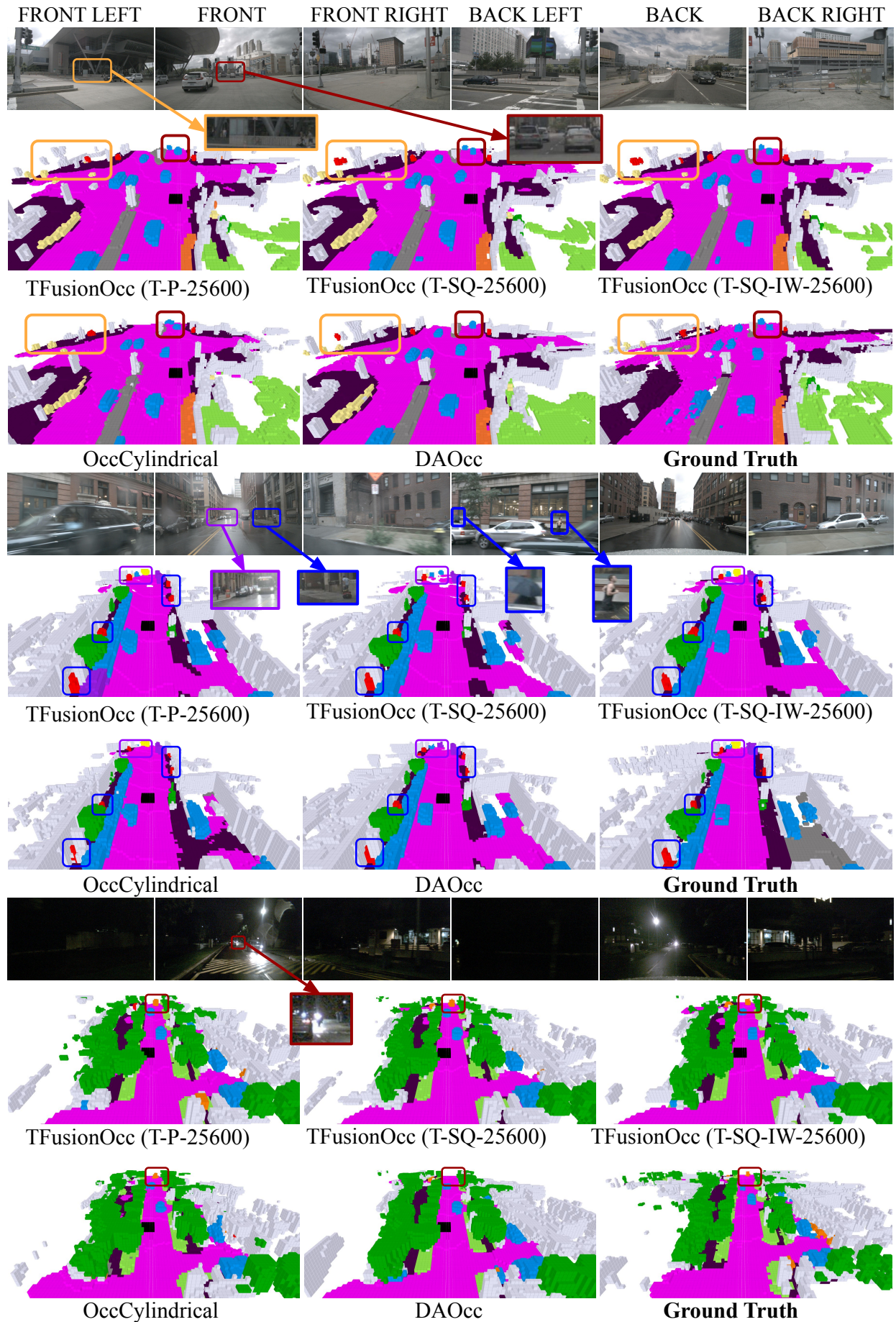


Fig. 13: Qualitative results compare against other SOTA algorithms for daytime, rainy, and nighttime scenarios displayed in the upper, middle, and bottom sections, respectively. **Better viewed when zoomed in.**

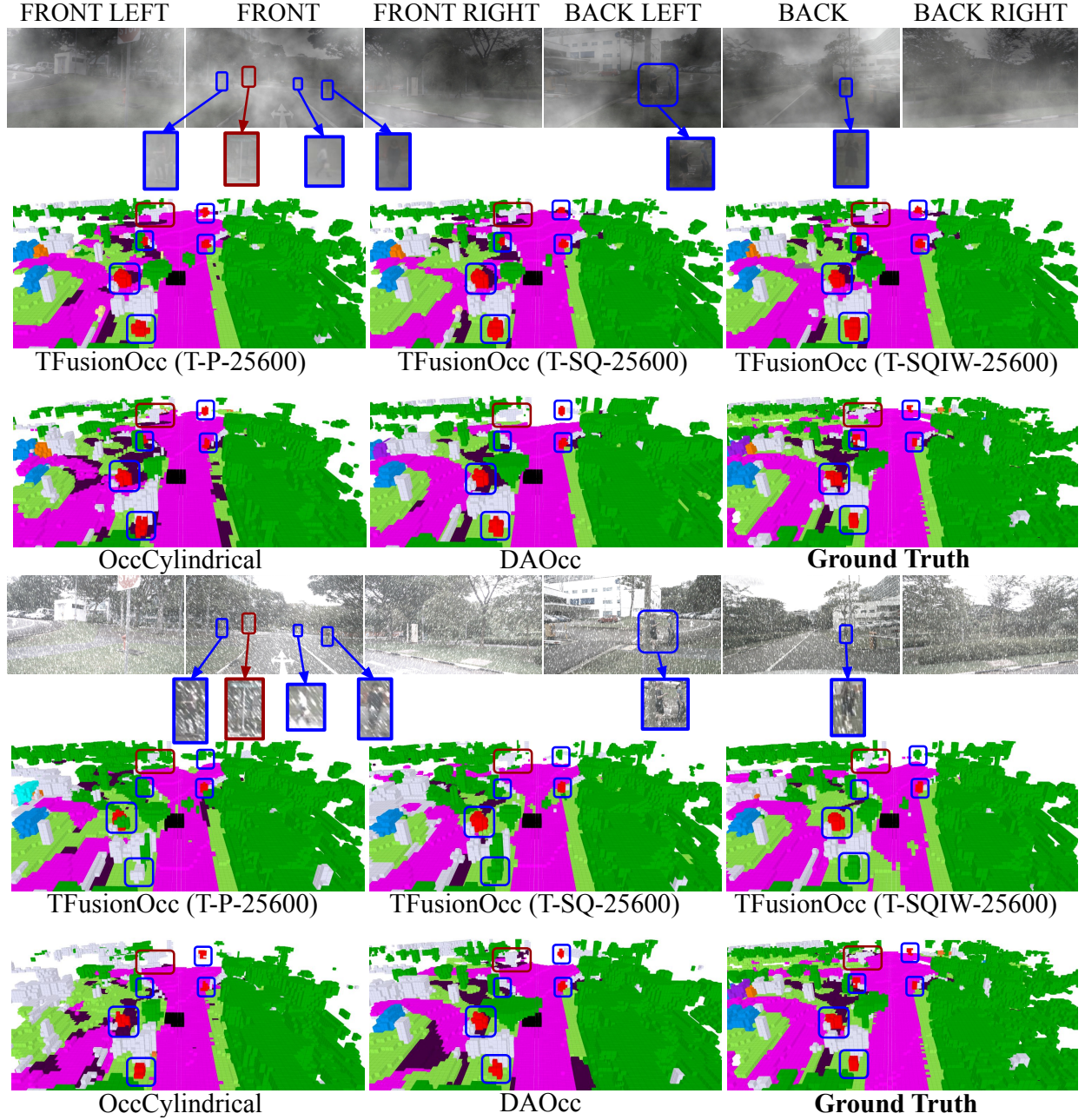


Fig. 14: Qualitative results compare against other SOTA algorithms under fog and snow scenarios, displayed in the top and bottom sections, respectively. **Better viewed when zoomed in.**

Range Filter r	IoU (\uparrow)	mIoU (\uparrow)
5 m	46.24 (Baseline)	30.79 (Baseline)
4 m	46.21 (-0.03%)	30.75 (-0.04%)
3 m	46.09 (-0.15%)	30.76 (-0.03%)
2 m	45.72 (-0.52%)	30.69 (-0.10%)
1 m	44.64 (-1.60%)	30.32 (-0.47%)
0.5 m	43.60 (-2.64%)	30.04 (-0.75%)

TABLE XIV: Ablation study on range filter hyperparameter r . \uparrow :the higher, the better.

1) *Ablation Study On Skeleton Merge Module:* We conducted an ablation study for each component of the skeleton merge module and demonstrated the results of the experiment

in Table XIII. The experiment results prove the significant impact of the main skeleton structure, which supports the fundamental 29.92% mIoU and 41.96% IoU performance, and the auxiliary impact of the augment structure, which further boosts 0.87% mIoU and 4.28% IoU performance. The main skeleton, based on lidar, provides detailed 3D geometric information of the surrounding scene, and the augmented skeleton, based on the camera, provides additional information to mitigate occlusion impact in the scene. Furthermore, we studied the impact of the range filter hyperparameter r on the overall performance of the model and present the results in Table XIV. The results show that a smaller filter range forces the augmented skeleton to get too close to the main skeleton,

Vis-Depth Fusion	Depth-Fusion	Vis-Depth	Lidar-Depth		IoU (\uparrow)	mIoU (\uparrow)
✓	✓	✓	✓		46.24 (Baseline)	30.79 (Baseline)
✓	✗	✓	✗		46.06 (-0.18%)	30.57 (-0.22%)
✓	✗	✗	✓		39.80 (-6.44%)	25.28 (-5.51%)
✗	✓	✓	✓		44.01 (-2.23%)	28.98 (-1.81%)
✗	✗	✓	✗		43.99 (-2.25%)	28.93 (-1.86%)
✗	✗	✗	✓		40.33 (-5.91%)	24.71 (-6.08%)

TABLE XV: Ablation study on Depth-Fusion-Based 3D Deformable Attention Module. \uparrow : the higher, the better. Vis-Depth Fusion: add the fused depth feature back to the visual feature, resulting in a depth-aware visual feature. Depth-Fusion: fuse the visual depth feature with the lidar depth feature. Vis-Depth: visual depth feature. Lidar-Depth: lidar depth feature. \uparrow : the higher, the better.

Skip-Connect	WSFusion	GCFusion		IoU (\uparrow)	mIoU (\uparrow)
✓	✓	✓		46.24 (Baseline)	30.79 (Baseline)
✓	✓	✗		38.60 (-7.64%)	18.18 (-12.61%)
✓	✗	✓		39.39 (-6.85%)	18.57 (-12.22%)
✗	✓	✓		24.20 (-22.04%)	19.91 (-10.88%)

TABLE XVI: Ablation study on the MGCAFusion Module. Skip-Connnet: skip-connection structure at the last feature fusion stage. WSFusion: weighted summation fusion part. GCFusion: gated concatenation fusion part. \uparrow : the higher, the better.

preventing it from overcoming the lidar sensor's occlusion limitation.

2) *Ablation Study On Depth-Fusion-Based 3D Deformable Attention Module*: We conducted an ablation study with respect to each component of the depth-fusion-based 3D deformable attention module and presented the experiment results in Table XV. In practice, Vis-Depth provides dense but less accurate depth maps, while Lidar-Depth provides sparse but more accurate depth maps. The experiment shows that dense depth maps contribute significantly to the performance, even though they are less accurate. Relying solely on sparse but accurate depth maps from lidar results in a significant performance degradation of 5.5%-6.0%. Furthermore, adding fused depth maps back to the original visual features results in depth-aware visual features contributing the second-largest performance improvement, around 2.2%. The experiment results demonstrate the necessity of multi-stage multi-modality feature fusion to boost model performance.

3) *Ablation Study On MGCAFusion Module*: We conducted an ablation study for each major component of the MGCAFusion module and present the experiment results in Table XVI. The experiment results show that the weighted summation and gated concatenation fusion components contribute almost equally to the model's final performance, with the former slightly more important. Missing each part will cause 12.22% to 12.61% mIoU and 6.85% to 7.64% IoU performance degradation. The skip-connection structure plays an important role during the feature fusion.

V. CONCLUSION AND FUTURE WORK

This paper presents TFusionOcc, a novel Student's t-distribution-based object-centric multi-stage multi-sensor fusion framework. Our framework in the sensor fusion part adopts a multi-stage feature-level fusion strategy, including an early-stage, a middle-stage, and a late-stage fusion, to better integrate complementary information across modalities and

mitigate the drawbacks of each modality. We also adopt an object-centric modeling strategy by leveraging the Student's t-distribution and the T-Mixture model as a probability kernel, combined with several typical primitives, such as the general T-Primitive and the superquadric, to achieve greater robustness against outliers. We further propose a primitive called the deformable superquadric primitive (superquadric with inverse-warp), which offers greater geometric shape representation flexibility, thereby boosting the model's 3D geometric shape-capturing capability in the driving scene. The extensive experiments conducted on the nuScenes [10] and nuScenes-C [11] datasets, including challenging cases of rainy, night, fog, snow and sensor-malfunction, demonstrate that our proposed approach not only achieves SOTA performance but also exhibits superior robustness. In our future research endeavors, we will investigate how to utilize a much smaller set of primitives and fewer rendering operations to achieve similar performance.

REFERENCES

- [1] Z. Ming, J. S. Berrio, M. Shan, and S. Worrall, "Occfusion: Multi-sensor fusion framework for 3d semantic occupancy prediction," *IEEE Transactions on Intelligent Vehicles*, 2024.
- [2] J. Pan, Z. Wang, and L. Wang, "Co-occ: Coupling explicit feature fusion with volume rendering regularization for multi-modal 3d semantic occupancy prediction," *IEEE Robotics and Automation Letters*, 2024.
- [3] S. Zhang, Y. Zhai, J. Mei, and Y. Hu, "Fusionocc: Multi-modal fusion for 3d occupancy prediction," in *Proceedings of the 32nd ACM International Conference on Multimedia*, 2024, pp. 787–796.
- [4] Z. Ming, J. S. Berrio, M. Shan, Y. Huang, H. Lyu, N. H. K. Tran, T.-Y. Tseng, and S. Worrall, "Occylindrical: Multi-modal fusion with cylindrical representation for 3d semantic occupancy prediction," *arXiv preprint arXiv:2505.03284*, 2025.
- [5] Z. Yang, Y. Dong, J. Wang, H. Wang, L. Ma, Z. Cui, Q. Liu, H. Pei, K. Zhang, and C. Zhang, "Daocc: 3d object detection assisted multi-sensor fusion for 3d occupancy prediction," *IEEE Transactions on Circuits and Systems for Video Technology*, 2025.
- [6] Z. Duan, C. Dang, X. Hu, P. An, J. Ding, J. Zhan, Y. Xu, and J. Ma, "Sdgocc: Semantic and depth-guided bird's-eye view transformation for 3d multimodal occupancy prediction," in *Proceedings of the Computer Vision and Pattern Recognition Conference*, 2025, pp. 6751–6760.
- [7] Y. Shi, K. Jiang, J. Miao, K. Wang, K. Qian, Y. Wang, J. Li, T. Wen, M. Yang, Y. Xu *et al.*, "Effocc: Learning efficient occupancy networks from minimal labels for autonomous driving," *arXiv preprint arXiv:2406.07042*, 2024.
- [8] L. Zhao, S. Wei, J. Hays, and L. Gan, "Gaussianformer3d: Multi-modal gaussian-based semantic occupancy prediction with 3d deformable attention," *arXiv preprint arXiv:2505.10685*, 2025.
- [9] T. Pavković, M.-A. N. Mahani, J. Niedermayer, and J. Betz, "Gaussianfusionocc: A seamless sensor fusion approach for 3d occupancy prediction using 3d gaussians," *arXiv preprint arXiv:2507.18522*, 2025.
- [10] H. Caesar, V. Bankiti, A. H. Lang, S. Vora, V. E. Liou, Q. Xu, A. Krishnan, Y. Pan, G. Baldan, and O. Beijbom, "nuscenes: A multimodal dataset for autonomous driving," in *Proceedings of the IEEE/CVF conference on computer vision and pattern recognition*, 2020, pp. 11621–11631.
- [11] S. Xie, L. Kong, W. Zhang, J. Ren, L. Pan, K. Chen, and Z. Liu, "Benchmarking and improving bird's eye view perception robustness in autonomous driving," *IEEE Transactions on Pattern Analysis and Machine Intelligence*, 2025.
- [12] B. Mildenhall, P. P. Srinivasan, M. Tancik, J. T. Barron, R. Ramamoorthi, and R. Ng, "Nerf: Representing scenes as neural radiance fields for view synthesis," *Communications of the ACM*, vol. 65, no. 1, pp. 99–106, 2021.
- [13] Z. Ming, J. S. Berrio-Perez, M. Shan, and S. Worrall, "Inverse++: Vision-centric 3d semantic occupancy prediction assisted with 3d object detection," *Neurocomputing*, p. 132162, 2025.
- [14] Y. Huang, W. Zheng, Y. Zhang, J. Zhou, and J. Lu, "Gaussianformer: Scene as gaussians for vision-based 3d semantic occupancy prediction," in *European Conference on Computer Vision*. Springer, 2024, pp. 376–393.

[15] Y. Huang, A. Thammatadatrakoon, W. Zheng, Y. Zhang, D. Du, and J. Lu, "Gaussianformer-2: Probabilistic gaussian superposition for efficient 3d occupancy prediction," in *Proceedings of the Computer Vision and Pattern Recognition Conference*, 2025, pp. 27477–27486.

[16] B. Kerbl, G. Kopanas, T. Leimkühler, and G. Drettakis, "3d gaussian splatting for real-time radiance field rendering," *ACM Trans. Graph.*, vol. 42, no. 4, pp. 139–1, 2023.

[17] S. Zuo, W. Zheng, X. Han, L. Yang, Y. Pan, and J. Lu, "Quadricformer: Scene as superquadrics for 3d semantic occupancy prediction," *arXiv preprint arXiv:2506.10977*, 2025.

[18] H. Zhou, X. Zhu, X. Song, Y. Ma, Z. Wang, H. Li, and D. Lin, "Cylinder3d: An effective 3d framework for driving-scene lidar semantic segmentation," *arXiv preprint arXiv:2008.01550*, 2020.

[19] K. He, X. Zhang, S. Ren, and J. Sun, "Deep residual learning for image recognition," in *Proceedings of the IEEE conference on computer vision and pattern recognition*, 2016, pp. 770–778.

[20] Y. Yan, Y. Mao, and B. Li, "Second: Sparsely embedded convolutional detection," *Sensors*, vol. 18, no. 10, p. 3337, 2018.

[21] H. Zhao, L. Jiang, J. Jia, P. H. Torr, and V. Koltun, "Point transformer," in *Proceedings of the IEEE/CVF International Conference on Computer Vision*, 2021, pp. 16 259–16 268.

[22] H. Li, H. Zhang, Z. Zeng, S. Liu, F. Li, T. Ren, and L. Zhang, "Dfa3d: 3d deformable attention for 2d-to-3d feature lifting," in *Proceedings of the IEEE/CVF International Conference on Computer Vision*, 2023, pp. 6684–6693.

[23] T. Wang, X. Zhu, J. Pang, and D. Lin, "Fcos3d: Fully convolutional one-stage monocular 3d object detection," in *Proceedings of the IEEE/CVF International Conference on Computer Vision*, 2021, pp. 913–922.

[24] M. Berman, A. R. Triki, and M. B. Blaschko, "The lovász-softmax loss: A tractable surrogate for the optimization of the intersection-over-union measure in neural networks," in *Proceedings of the IEEE conference on computer vision and pattern recognition*, 2018, pp. 4413–4421.

[25] Y. Wei, L. Zhao, W. Zheng, Z. Zhu, J. Zhou, and J. Lu, "Surroundocc: Multi-camera 3d occupancy prediction for autonomous driving," in *Proceedings of the IEEE/CVF International Conference on Computer Vision*, 2023, pp. 21 729–21 740.

[26] X. Tian, T. Jiang, L. Yun, Y. Mao, H. Yang, Y. Wang, Y. Wang, and H. Zhao, "Occ3d: A large-scale 3d occupancy prediction benchmark for autonomous driving," *Advances in Neural Information Processing Systems*, vol. 36, pp. 64 318–64 330, 2023.

[27] A.-Q. Cao and R. de Charette, "Monoscene: Monocular 3d semantic scene completion," in *Proceedings of the IEEE/CVF Conference on Computer Vision and Pattern Recognition*, 2022, pp. 3991–4001.

[28] Z. Murez, T. Van As, J. Bartolozzi, A. Sinha, V. Badrinarayanan, and A. Rabinovich, "Atlas: End-to-end 3d scene reconstruction from posed images," in *Computer Vision–ECCV 2020: 16th European Conference, Glasgow, UK, August 23–28, 2020, Proceedings, Part VII 16*. Springer, 2020, pp. 414–431.

[29] Z. Li, W. Wang, H. Li, E. Xie, C. Sima, T. Lu, Y. Qiao, and J. Dai, "Bevformer: Learning bird's-eye-view representation from multi-camera images via spatiotemporal transformers," in *ECCV*. Springer, 2022, pp. 1–18.

[30] Y. Huang, W. Zheng, Y. Zhang, J. Zhou, and J. Lu, "Tri-perspective view for vision-based 3d semantic occupancy prediction," in *Proceedings of the IEEE/CVF Conference on Computer Vision and Pattern Recognition*, 2023, pp. 9223–9232.

[31] X. Wang, Z. Zhu, W. Xu, Y. Zhang, Y. Wei, X. Chi, Y. Ye, D. Du, J. Lu, and X. Wang, "Openoccupancy: A large scale benchmark for surrounding semantic occupancy perception," in *Proceedings of the IEEE/CVF International Conference on Computer Vision*, 2023, pp. 17 850–17 859.

[32] Z. Ming, J. S. Berrio, M. Shan, and S. Worrall, "Inversematrixvt3d: An efficient projection matrix-based approach for 3d occupancy prediction," in *2024 IEEE/RSJ International Conference on Intelligent Robots and Systems (IROS)*. IEEE, 2024, pp. 9565–9572.

[33] Y. Zhang, Z. Zhu, and D. Du, "Occformer: Dual-path transformer for vision-based 3d semantic occupancy prediction," in *Proceedings of the IEEE/CVF International Conference on Computer Vision*, 2023, pp. 9433–9443.

[34] Z. Li, Z. Yu, D. Austin, M. Fang, S. Lan, J. Kautz, and J. M. Alvarez, "Fb-occ: 3d occupancy prediction based on forward-backward view transformation," *arXiv preprint arXiv:2307.01492*, 2023.

[35] M. Pan, J. Liu, R. Zhang, P. Huang, X. Li, H. Xie, B. Wang, L. Liu, and S. Zhang, "Renderocc: Vision-centric 3d occupancy prediction with 2d rendering supervision," in *2024 IEEE International Conference on Robotics and Automation (ICRA)*. IEEE, 2024, pp. 12 404–12 411.

[36] L. Roldao, R. de Charette, and A. Verroust-Blondet, "Lmscnet: Lightweight multiscale 3d semantic completion," in *2020 International Conference on 3D Vision (3DV)*. IEEE, 2020, pp. 111–119.

[37] J. Huang, G. Huang, Z. Zhu, Y. Ye, and D. Du, "Bevdet: High-performance multi-camera 3d object detection in bird-eye-view," *arXiv preprint arXiv:2112.11790*, 2021.

[38] Y. Li, H. Bao, Z. Ge, J. Yang, J. Sun, and Z. Li, "Bevstereo: Enhancing depth estimation in multi-view 3d object detection with temporal stereo," in *Proceedings of the AAAI Conference on Artificial Intelligence*, vol. 37, no. 2, 2023, pp. 1486–1494.

[39] H. Zhang, X. Yan, D. Bai, J. Gao, P. Wang, B. Liu, S. Cui, and Z. Li, "Radocc: Learning cross-modality occupancy knowledge through rendering assisted distillation," in *Proceedings of the AAAI Conference on Artificial Intelligence*, vol. 38, no. 7, 2024, pp. 7060–7068.

[40] Y. Ren, L. Wang, M. Li, H. Jiang, Z. Cui, M. Yang, H. Yu, and D. Yang, "Rm 2 occ: Re-projection multi-task multi-sensor fusion for autonomous driving 3d object detection and occupancy perception," *IEEE Transactions on Intelligent Transportation Systems*, 2025.